Computational modeling of yielding octagonal connection for concentrically braced frames

F. Nejati, M. Zhian, F. Safar Mashaie, S.A. Edalatpanah*
Ayandegan Institute of Higher Education, Tonekabon, Iran
* E-mail: saedalatpanah@gmail.com

Abstract. Ductility is a feature which allows a structure to undergo large plastic deformations without any strength loss. Yield dampers are energy dissipation devices which increase the ductility and control the vibration of structures by absorbing earthquake input energy. If a structure is properly designed according to the standard, if a severe earthquake occurs, it will cause serious damage to the structure. If this happens in a massive city, thousands of people are homeless and need to evacuate the debris that it seems impossible to do. Therefore, the design of systems that lead the damage to a certain part of structures is required. Incorporating an energy-dissipater element in the braces is one of the novel approaches to increase the ductility of the braces. This study aims to assess the influence of design parameters related to the energy absorption device on the seismic response of CBFs. These factors include the yield strength, initial stiffness, and strain hardening ratio. Thus a regular octagonal-shaped energy absorption device is introduced, which enters the non-linear range by steel yielding in order to dissipate the earthquake input energy and prevent other structural members from entering the plastic region. The proposed device can be called Yielding Octagonal Connection (YOC), which is modeled using Abaqus finite element software and exposed to cyclic loading according to the ATC-24 code. A bilinear stress-strain curve for steel is used for the modeling. When the hysteresis and envelope curves are obtained, the structure equipped with YOCs is designed using SAP2000. To investigate the behavior of this energy absorption device, a non-linear time history analysis (NLTHA) is conducted for 16-storey steel structures with regular plans and concentrically braced frames (CBFs) under near- and far-field earthquakes. The results of analyses indicate 68 % and 65 % decrease in the maximum base reaction, 79 % and 82 % decrease in the maximum roof story acceleration, 60 % and 58 % decrease in the maximum displacement at roof level under near and far-field earthquakes, respectively.

1. Introduction

Seismic design codes are generally accepted to repair the structures after major earthquakes. Members of a structure deformed against earthquake forces and dissipate the energy of an earthquake. When the earthquake forces rise to an extent, causing important structural members to have plastic joints. Since the repair of the important members of the structure is very difficult and sometimes impossible after earthquake In order to provide a repairable building, "Directed Damage Design" idea can be used, which means guiding damages to predetermined specific points of structure so that the damage of primary and secondary structural members is reduced by the concentration of plastic regions on these points. Yield dampers provide a suitable solution to focus damage on specific parts of the structural system. The mechanism of these dampers is based on increasing the energy absorption by concentrating a major part of plastic regions on them due to the nature of inelastic behavior, improving the seismic performance of the structure against ground motions. This paper proposes a new seismic damper based on the yielding of metals and compares its performance to a Special Concentrically Braced Frame «SCBF» through non-linear dynamic analyses. It can be easily installed like a conventional brace and strength and stiffness can be adjusted independently. To validate the applicability of the proposed damper design, a series of cyclic load tests on the damper were conducted. The cyclic behavior of the damper was determined by finite element method. The following researches have indicated a number of performance issues with respect to some of yielding dampers.

Added damping and stiffness (ADAS) and triangular added damping and stiffness (TADAS) dampers can be mentioned amongst these dampers. Franco et al. [1] proposed a yield damper whose performance mechanism was based on the plasticity properties of metals under twisting contact stress. This device comprised a tube of different cross-sections with lower thickness and diameter at middle parts. Hence the tube displacements were limited, and it would be allowed only to twist, improving the seismic resistance of structure by energy dissipation. In the same year, Mistakidis [2] numerically analyzed shear wall panels using low-yield-point (LYP) steel to retrofit and improve the seismic behavior of structures. Benavent-Climent [3] also introduced a brace-type damper consisted of a tube-in-tube assemblage of hollow sections. Its outer section comprised strips created by cutting a series of slits through the wall and the strips dissipated earthquake energy by flexural-shear yielding. Other studies were conducted by Ward et al. [4] investigated the Cast Modular Ductile Bracing System (CMDB) is under development as an alternative to special concentrically braced frames. This system introduces cast components at the ends and center of the brace in an attempt to produce a system with reliable strength, stiffness, and deformation capacity. A cruciform cross-section has been chosen for the cast component geometry, which is specially detailed to enhance energy dissipation and increase low cycle fatigue life thereby reducing the likelihood of fracture. Gray et al. [5] proposed a new cast steel yielding brace system which was a type of high-ductility braces with unique characteristics. In this system, the fingers of a specially engineered cast steel connection dissipate seismic energy by yielding. In another research, Beheshti-Aval et al. [6] studied a combination of circular damper and friction connection installed in the center of X-bracing systems. Hong-Nan Li and Gang Li [7] presented a dual friction metallic damper experimentally that have appropriate energy dissipation capabilities. Nejati et al. [8] assessed the performance of yield dampers in a steel structure through rocking (see-saw) motion. The results suggested that it is possible to dramatically reduce the damage of the structure using the damper and hence the structural system can be easily repaired after major earthquakes. Hsu and Halim [9] introduced a new brace design that adopted curved steel dampers with amplified deformation mechanisms. Marco Baiguera et al [10] studied on a dual seismic-resistant steel frame, which consists of a moment-resisting frame equipped with high post-yield stiffness energy-dissipative braces for residual drift reduction. Tiyari et al [11] proposed a new bracing system that consists of U-shaped elements as energy dissipation devices that can be considered as a hysteretic damper, which combines the advantages of the yielding dampers and the buckling resistant braces «BRB». Jarrah et al [12] introduced a new metallic damper which is comprised of a set of parallel hollow circular plates that can be installed in a structure within V-braces or diagonal braces.

The presented researches show the good performance of yield dampers as energy absorption devices that can reduce damage to other structural members by the concentration of failures on themselves. These systems can be used in both the design of new construction and retrofitting of existing buildings. In this paper, a regular octagonal energy absorption device is introduced, and its modeling process is described using Abaqus finite element software. The proposed device can be called Yielding Octagonal Connection (YOC). This damper is evaluated in the Concentrically Braced Frames system under the near- and far-field earthquakes by SAP2000 software [13].

2. Methods

2.1. Finite Element Simulation of YOCs

The proposed energy absorption device YOC is made of ST37 steel (equivalent to A283 in ASTM standard [14]), 15 cm in outer dimension, 1.5 cm in thickness and 15 cm in length. Two $20 \times 15 \times 1.5$ cm^3 connection plates were also connected to the YOC with a fillet weld. The octagonal element and connection plates were merged together and the simulation of the weld is neglected in the current study assuming that failure does not occur in the welds. The geometric shape of the yield damper is illustrated in Figure 1(a). As shown in Figure 1(b), the YOC is located at the point where the brace is connected to the top gusset plate of the frame.

YOC is modeled as a deformable, 3-dimensional, solid and homogeneous element, indicating the homogeneity and constancy of density throughout the components, and assessed through general and static analyses. Non-linear geometric deformations (large deformations) are applied in all steps of the analysis. The specifications of the steel used are given in Table 1 according to A283 in ASTM standard [14]).

The YOC is modeled using an 8-node linear brick element with reduced integration and hour-glass control (C3D8R). The C3D8R is defined as three-dimensional, hexahedral, eight-node linear brick, with reduced integration with hourglass control and first-order (linear) interpolation. Reduced integration uses a lower-order integration to form the elements stiffness which greatly reduces computation time. The first-order element is highly suggested when large strains have happened. A mesh size of 4 mm was utilized in the finite element simulation. Figure 2 shows the mesh of YOC.
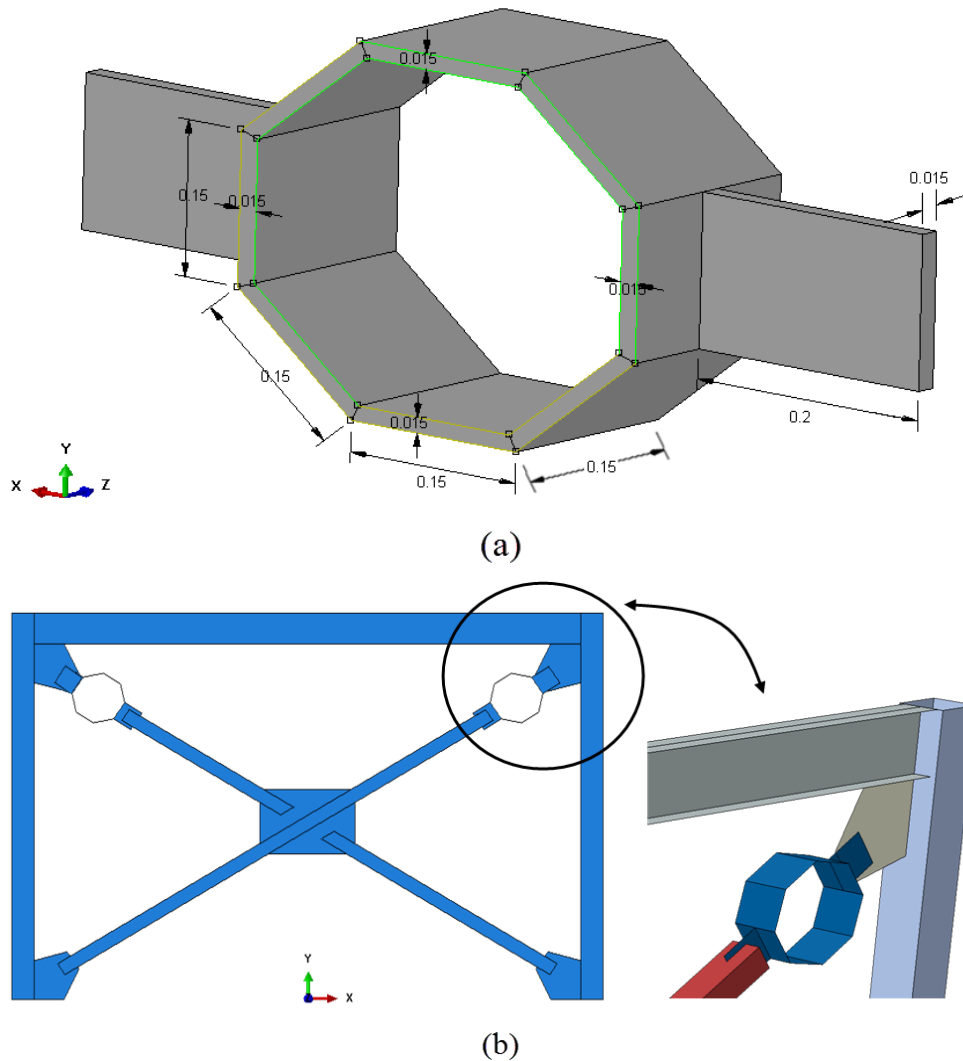
(a)

(b)

Figure 1. Geometric dimensions [m] of YOC (a), Position of YOC in the braced frame (b).

Table 1. Steel specifications.

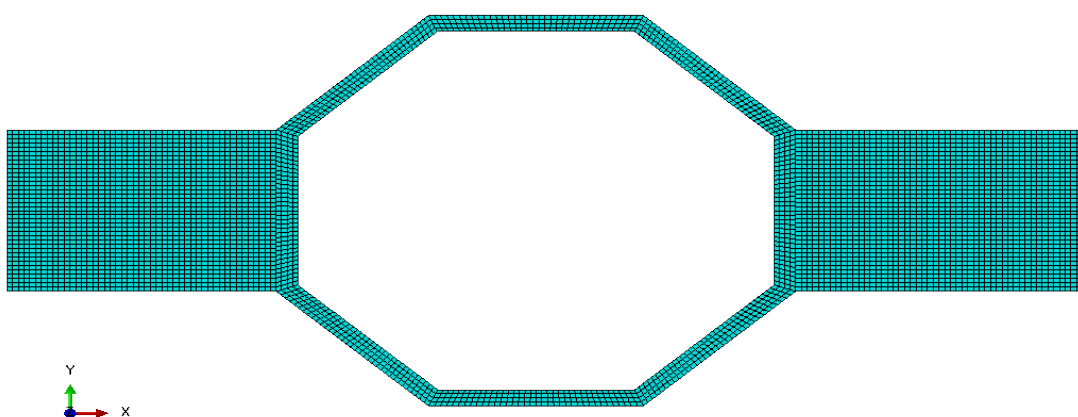| Density (kg/m³)	Modulus of Elasticity (GPa)	Poisson's Ratio	Yield Strength (MPa)	Ultimate Strength (MPa)	Ultimate Strain
7850	200	0.3	240	370	0.2

Figure 2. The meshing of YOC for Finite Element Analysis.

The cyclic loading protocol is applied according to the ATC-24 code [15] in order to examine the performance of YOC under cyclic loads. A displacement-controlled loading calculated based on the yielding displacement of the model is used in the current study. Figure 3 presents the loading sequence applied to the model, where δ_i is the maximum displacement at the ith cycle of loading history and n_i is the number of cycles with the peak of δ_i and Δ is yielding displacement of the energy absorbing device. The fixed boundary conditions and cyclic loading are defined for both opposite sides of the octagonal device. Also, in Figure 4 the support conditions and loading direction are displayed.
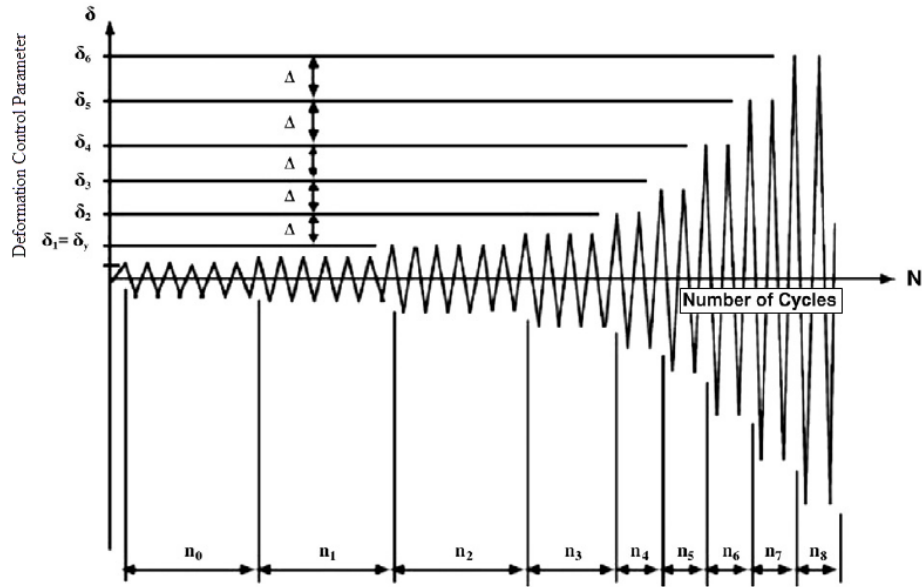
Nejati, F., Zhian, M., Safar Mashaie, F., Edalatpanah, S.A.

Figure 3. Loading protocol according to the ATC-24 code [15].

Figure 4 shows the loading and boundary condition of YOC. It should be mention that all degrees of freedom are restrained on boundary conditions.
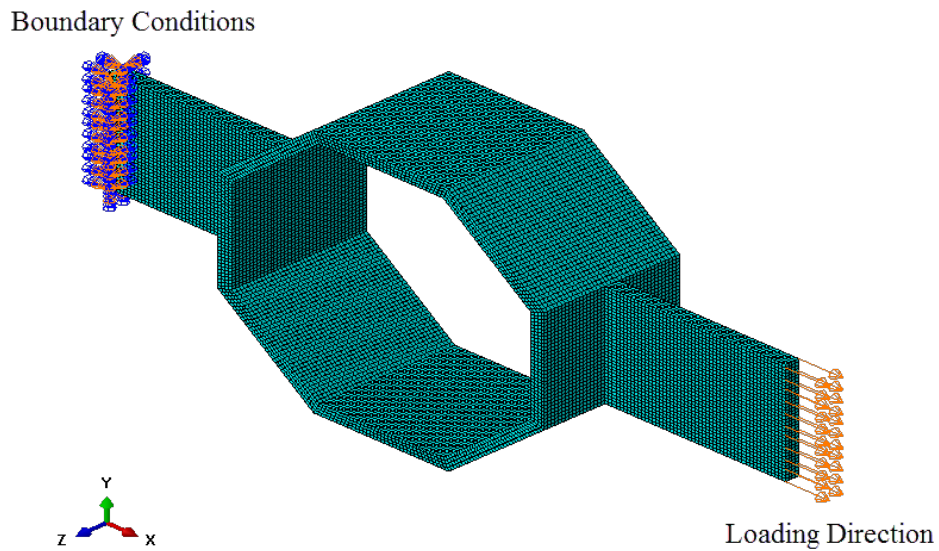

Figure 4. Boundary conditions and loading of YOC.

Figure 5 shows the von Mises stresses in YOC under the cyclic loading. The load-displacement diagram of the model is presented in Figure 6. The model was pushed until the peak strain reached the ultimate strain. The maximum tension and compression forces were 141.65 kN and 119.38 kN, respectively.
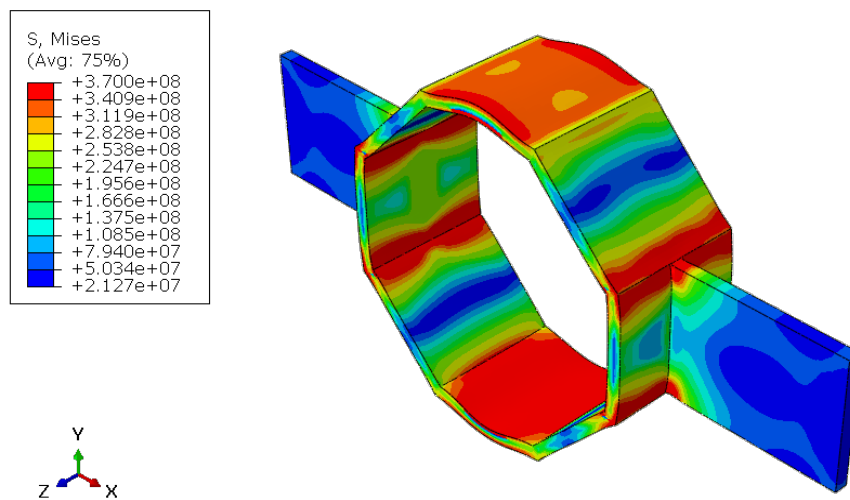
Figure 5. von Mises stress distribution in YOC (Pa).

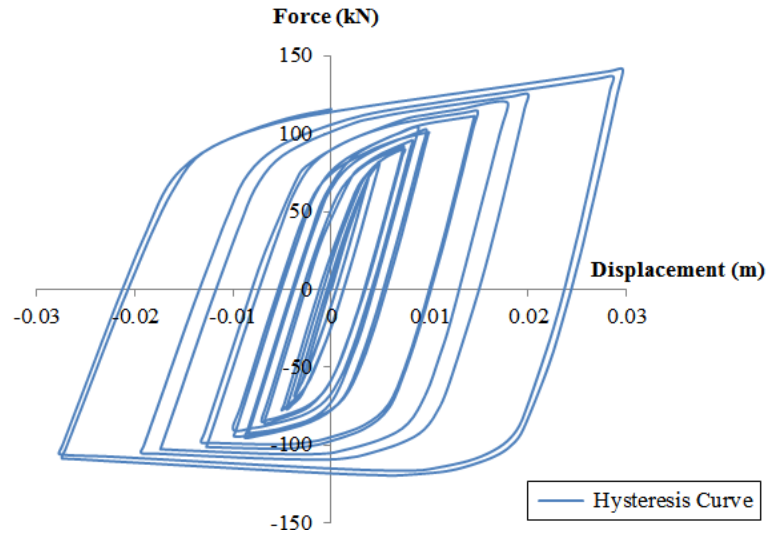Nejati, F., Zhian, M., Safar Mashaie, F., Edalatpanah, S.A.

Figure 6. Force-displacement hysteresis curve of YOC.

The envelope of the hysteretic response of the YOC is presented in Figure 7. As can be seen in this figure, the maximum displacement and corresponding displacement of the system at the end of the tensile elastic limit are 29.6 mm and 4.9 mm, respectively, based on two linearization method of FEMA 356 [16]. Similarly, the aforementioned parameters under the compression force were 27.7 mm and 4.6 mm, respectively. Therefore, the ductility of the model (μ) in tension and compression can be calculated, where Δ_{max} is the maximum deformation at failure and Δ_y is the deformation when the material or member yields.

$$\mu_T = \frac{\Delta_{Max}}{\Delta_y} = \frac{29.6}{4.9} = 6.04; \tag{1}$$

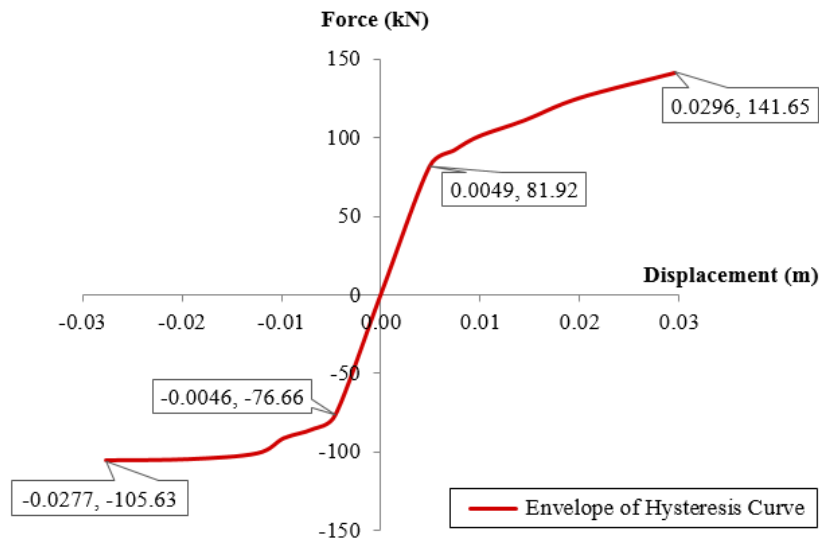$$\mu_C = \frac{\Delta_{Max}}{\Delta_y} = \frac{27.7}{4.6} = 6.02. \tag{2}$$

Figure 7. Hysteresis loop push of force-displacement plot for YOC.

2.2. Verification of the FE model

An experimental test performed by Abbasnia et al. [17] was used to verify the accuracy of the simulation. The specimen consisted of a steel ring with an outer diameter of 220 mm, the thickness of 12 mm, and a length of 100 mm. Two 200×100×12 mm³ connection plates were also connected to the steel ring with a 7 mm fillet weld. Figure 8(a) presents the tested specimen and Figure 8(b) shows its Abaqus model.

In the first step, based on the experimental results, steel material properties were defined in the Abaqus software [18]. Figure 9 presents the steel stress-strain diagram for ring and plates. The steel rings and connection plates were merged together and simulation of the weld is neglected in the current study assuming that failure does not occur in the welds. Fixed boundary condition was applied to one end of the model while an axial force was applied to the other end to investigate the behavior of the model (Figure 10). A mesh size of 4 mm was utilized in the finite element simulation.
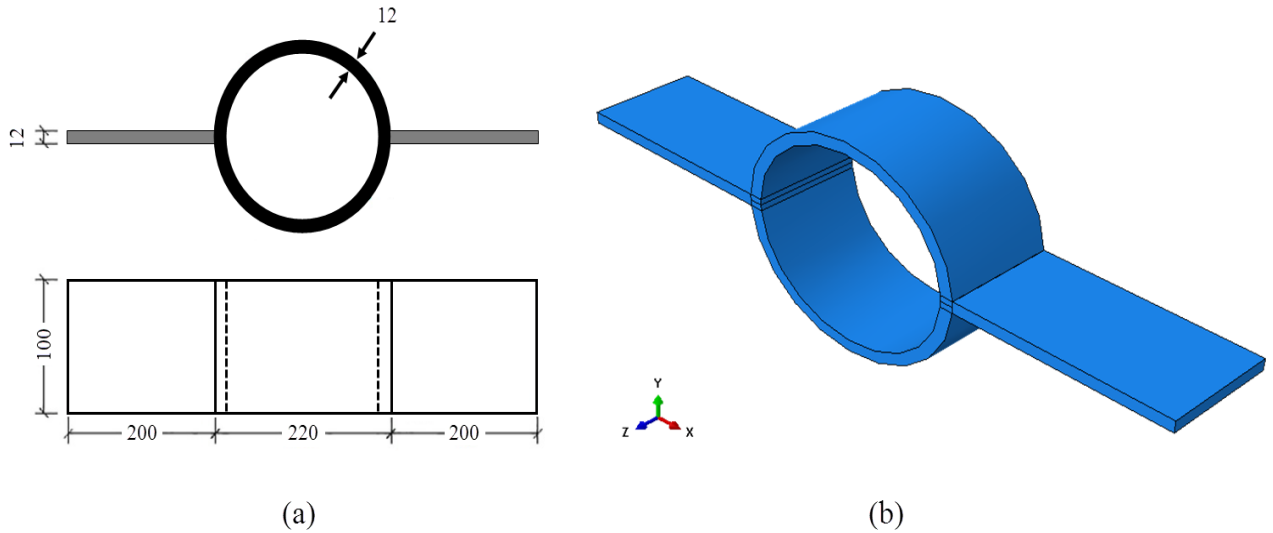
Nejati, F., Zhian, M., Safar Mashaie, F., Edalatpanah, S.A.

(a)   (b)

Figure 8. Dimensions [mm] of experimental specimen (a) analytical specimen (b).

(a)   (b)

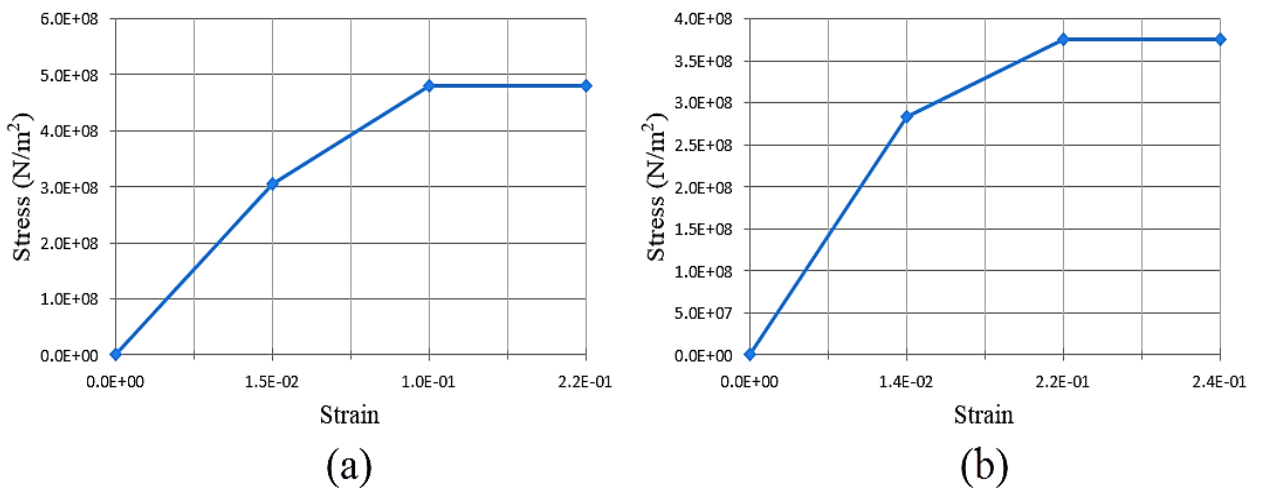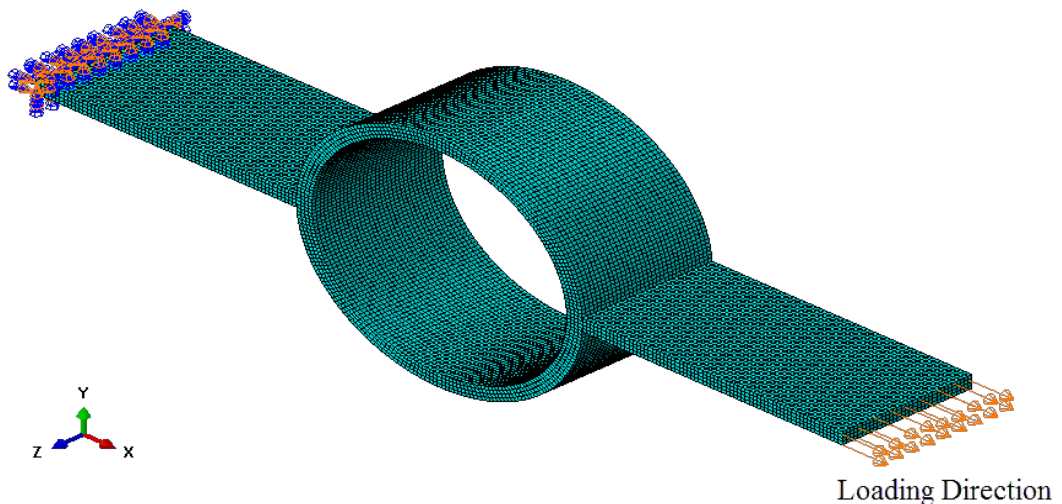**Figure 9. Steel Stress-strain diagram for the ring (a) and plates (b).**

**Figure 10. Boundary conditions and loading direction in Abaqus
for analytical specimen.**

Figure 11(a) illustrates how the steel ring was loaded by a hydraulic universal jack with a capacity of 700 kN of compressive and tensile strength. In addition to the applied axial force, the jacks measured the diameter of the ring. Figures 11(b) and 11(c) show the steel rings in pre-failure cycles in tensile and compression states, respectively.

Figure 12 shows von Mises stresses under a cyclic load for the steel ring in Abaqus.
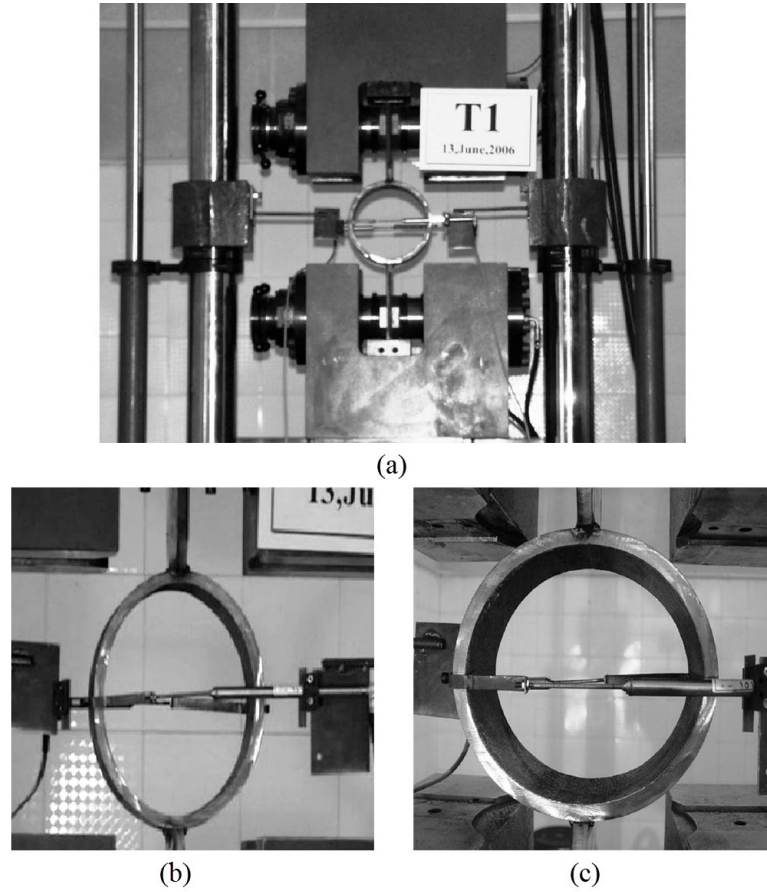
(a)

(b)   (c)

Figure 11. Hydraulic Universal Jack (a), Steel ring in tension (b), Steel ring in compression (c) [17].

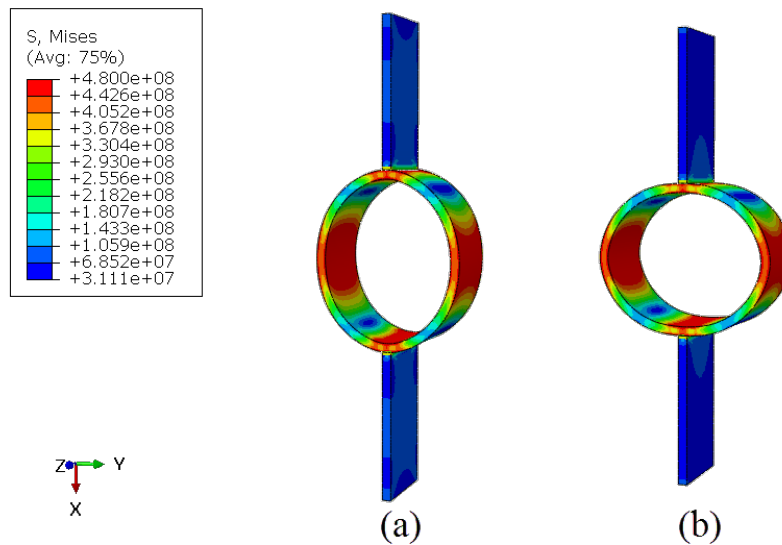(a)   (b)

Figure 12. von Mises stress distribution [Pa] in the steel ring in tension (a) and compression (b).

The load-displacement in experimental analysis dependence of the simulated ring under cyclic loading is shown in Figure 13. The Model was pushed until the peak strain in the model reached the ultimate strain. The maximum displacement and corresponding displacement of the system at the end of the tensile elastic limit are 20.16 mm and 2.79 mm, respectively. On the other hand, the aforementioned parameters under the compression force were 19.93 mm and 3.09 mm, respectively. Also, the maximum tension and compression force sustained by the model was 87.74 kN and 73.39 kN, respectively. Therefore, the ductility of the model in tension and compression can be calculated. This value are expressing for simulation, such that:

$$\mu_T = \frac{\Delta_{Max}}{\Delta_y} = \frac{20.16}{2.79} = 7.23; \tag{3}$$

$$\mu_C = \frac{\Delta_{Max}}{\Delta_y} = \frac{19.93}{3.09} = 6.45. \tag{4}$$
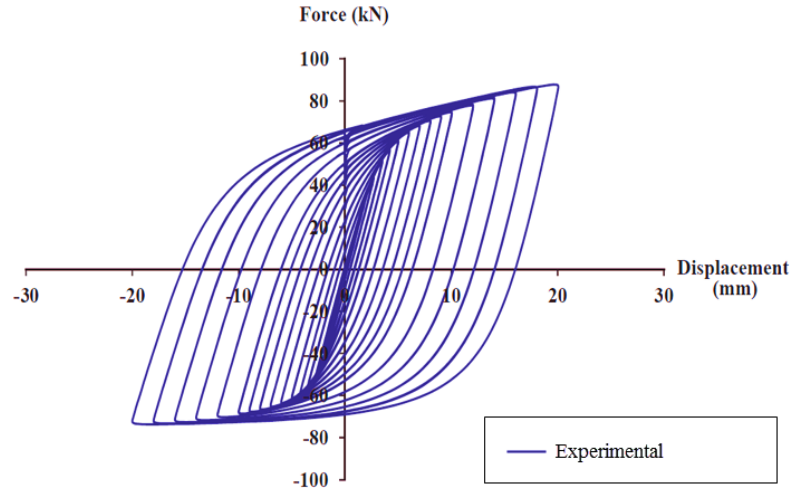
Figure 13. Force-displacement plot for experimental specimen [17].

The comparison between the numerical model and the experimental test, provided in Figure 14, demonstrated that the simulation can successfully predict the behavior of the tested steel ring and the results are in good agreement. Simulation results show that the maximum displacement and corresponding displacement of the system at the end of the tensile elastic limit are 20.37 mm and 2.53 mm, respectively. On the other hand, the aforementioned parameters under the compression force were 19.86 mm and 2.95 mm, respectively. Also, the maximum tension and compression force sustained by the model was 84.92 kN and 73.01 kN, respectively. Therefore, the ductility of the model in tension and compression can be calculated, such that:

$$\mu_T = \frac{\Delta_{max}}{\Delta_y} = \frac{20.37}{2.53} = 8.05; \tag{5}$$

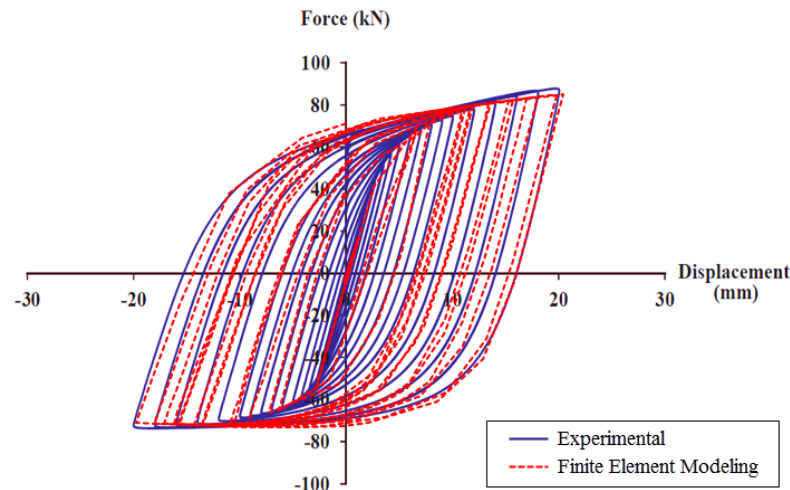$$\mu_C = \frac{\Delta_{max}}{\Delta_y} = \frac{19.86}{2.95} = 6.73. \tag{5}$$

Figure 14. Comparative hysteresis plots for finite element modeling and experimental results.

2.3. Specifications of the building

A 16-story steel structure with a regular plan and X-shaped bracing system is modeled 3-dimensionally in SAP2000 software to evaluate the performance of damper in the structure. The building was designed based on the conventional provisions (Iranian Standard No.2800 [19], which is very similar to the UBC). The plan of the floors along with the locating of the braces is shown in Figure16 (a). The beams, columns, and braces are connected using pinned connections and the base of the structure is connected to the foundation using fixed connections. Moreover, IPE sections for the beams and hollow structural section (HSS) for the columns and braces are determined. The gravity load is included in dead and live loads. According to the building executive plans, the dead and live load of the story floors are considered equal to 700 kg/m² and 200 kg/m². Also the dead and live load of the roof floor are considered equal to 650 kg/m² and 150 kg/m². The other types of loading including a wind load, a snow load, and also the load from soil–structure interaction have not been considered. The concrete deck compressive strength and thickness have been considered equal to 200 MPa and 15 cm, respectively. The cross-section specifications are summarized in Table 2.

Nejati, F., Zhian, M., Safar Mashaie, F., Edalatpanah, S.A.

Table 2. Specifications of cross-sections.

Number of stories	Column		Brace	Beam
	Other	Bay of bracing		
1	BOX 400×400×25	BOX 520×520×25		
2	BOX 400×400×25	BOX 450×450×25	BOX 160×160×10	IPE 240
3–6	BOX 400×400×25	BOX 400×400×25		
7, 8	BOX 340×340×20	BOX 340×340×20		
9, 10	BOX 280×280×16	BOX 280×280×16	BOX 140×140×10	IPE 220
11	BOX 200×200×16	BOX 200×200×16		
12	BOX 200×200×16	BOX 200×200×16	BOX 120×120×10	
13, 14	BOX 160×160×10	BOX 160×160×10		IPE 200
15, 16	BOX 120×120×10	BOX 120×120×10	BOX 100×100×10	

Plastic hinges are assigned in SAP2000 software as follows: for the columns of the braced span, force-controlled actions (brittle elements) and axial force type plastic hinges are defined and assigned. For the brace members, deformation-controlled actions (ductile elements) and axial force type plastic hinges are assigned. The plastic hinges are defined in accordance with the ASCE 41-13 [20]. Figure 15 shows the generalized force-deformation curves and acceptance criteria for deformation-controlled actions. Acceptance criteria for deformation or deformation ratios for primary components "P" and secondary components "S" corresponding to the target Building Performance Levels of Collapse Prevention "CP", Life Safety "LS", and Immediate Occupancy "IO" as shown in Figure15. The portions of the hinge load-deformation curve from A to B are ignored by the SAP2000 software. In this range, the behavior of the element is linear and the hinge is colorless. After hinge yields at point B, plastic deformation is determined by the curve B-C-D-E with all plastic deformation measured relative to B. The hinge colors in the plastic region for ductile elements are shown in Table 3.
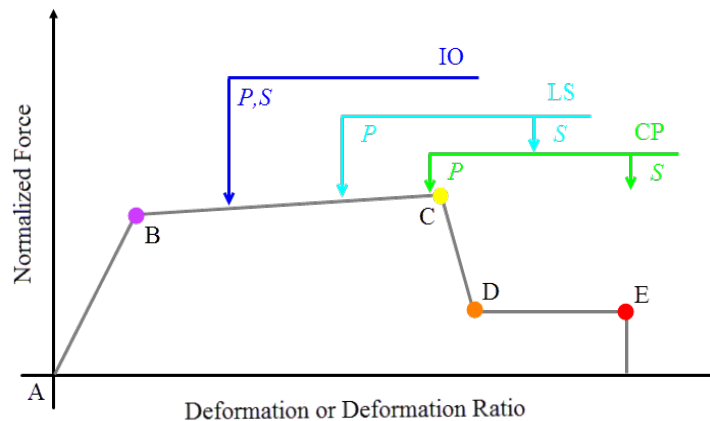
Figure 15. Generalized Component Force-Deformation Relations for deformation-controlled actions.

Table3. The hinge colors in the plastic region for ductile elements in SAP2000 software.

Hinge Status	Hinge Color
Before point B	Colorless
B to < IO	Purple
IO to < LS	Blue
LS to < CP	Turquoise
CP to < C	Green
C to < D	Yellow
D to < E	Orange
After Point E	Red

The SAP2000 force-controlled tool was employed to check the "Force/Maximum Allowed Force Ratio" of the structural members. The values of these ratios are specified by the user. There is no plastic area for the force-controlled actions (Brittle elements), then it is not necessary to consider the acceptance criteria for the brittle elements; however, the SAP2000 has chosen the same three colors as the acceptance criteria colors. Therefore, the brittle elements can have blue, turquoise, green, and red colors.

2.4. Using the proposed device in building frames

In order to model the proposed connection at the end of the brace, multi-linear plastic kinematic is used in SAP2000 software. This behavioral model, based on the kinematic hardening behavior commonly observed in metals, presents a non-linear force-deformation relationship under monotonic loading provided by a multi-linear curve described by a set of user-defined points, as seen in Figure 16(a). The first slope on each side of the origin is elastic and the remaining portions of the curve define plastic deformation. Upon reversals of deformation, the hysteresis path follows the two elastic segments of the curve from each side of the origin before initiating plastic deformation in the reverse direction. To appropriately illustrate the behavior of load reversal paths under cyclic loading of increasing magnitude, Figure 16(b) defines the origin as point 0, the points on the positive axis as 1, 2, 3 from the origin, and the points on the negative axis as –1, –2, –3 from the origin. The displacement and force values obtained from the YOC hysteresis curve for these 7 points are presented in Table 4.
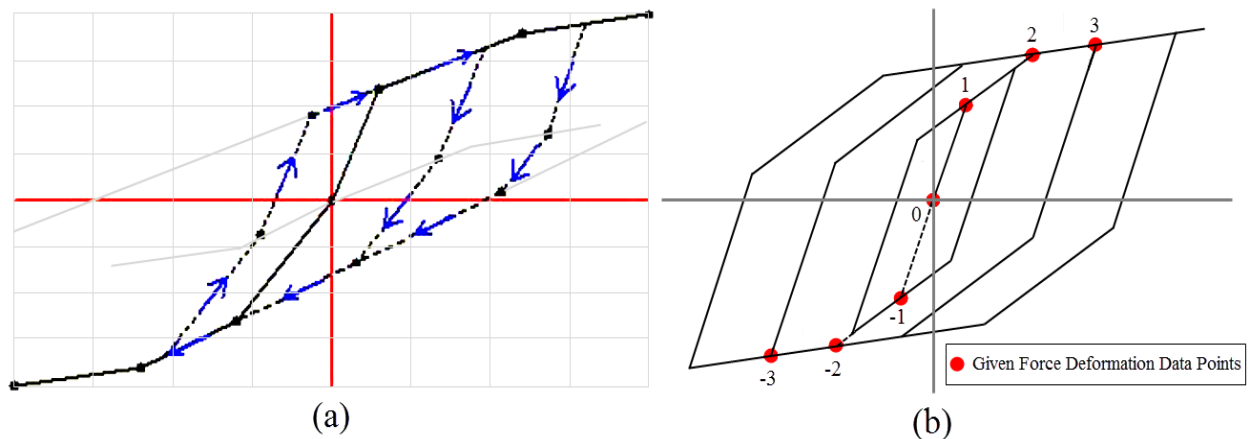

Figure 16. SAP2000 multi-linear kinematic plasticity property type for uniaxial deformation (a), SAP2000 behavior under cyclic loading of increasing magnitude for the multi-linear kinematic plasticity property type for uniaxial deformation (b).

*Table 4. Defined envelop curves for the multi-linear plastic link elements in SAP2000.*

Point	Displacement (mm)	Force (kN)
3	29.6	141.65
2	14.5	111.46
1	4.9	81.92
0	0	0
–1	4.6	76.66
–2	12.4	101.18
–3	27.7	105.63

The hysteresis envelope curve for the proposed damper is located within a 16-story steel structure equipped with a CBF system in order to evaluate the seismic performance of the damper in braced frames under near- and far-field earthquakes. Figure 17 shows the plan and the 3D view of the 16-story structure equipped with and without YOC schematically.
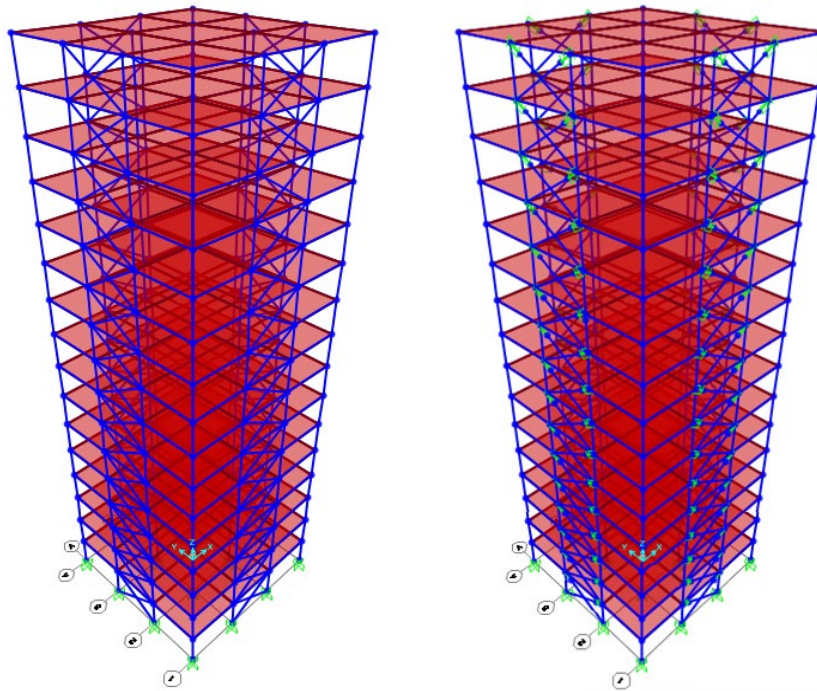
2.5. Specifications of applied earthquakes

Given the distance from a fault, recorded accelerations are classified as near-fault and far-fault earthquakes. If acceleration is recorded at a station within a distance of less than 15 km from the fault, it is generally called a near-fault motion, while that recorded within a further distance is called a far-fault motion. The distance from the fault is very important for selecting the acceleration, because it may lead to highly different responses of the structure. Thus three near-field and far-field accelerations are used for the Non-Linear Time History Analysis (NLTHA) in this study, whose specifications are given in Tables 5 and 6, respectively. The earthquake records have been scaled based on the method proposed by Section 2.4.2.2 ASCE 41-13 [20]. Therefore, the scale number obtained for the near- and far-field acceleration is equal to 0.4117 g and 0.4349 g, respectively. Ground motions used in this study were generated by PEER ground motion database [21]. Figure 18 shows the response spectra for the suite of ground motions. A Target response spectrum based on type II soil (The average shear wave shear rate «$\overline{v}_s$», Average Standard

Penetration Resistance «$\overline{N}_{1(60)}$» and Average Undrained Shear Strength «$\overline{C}_u$» are 700 m/s, 60 and 275 kPa, respectively) and very high risk in seismic regions of Iran have been selected [19].
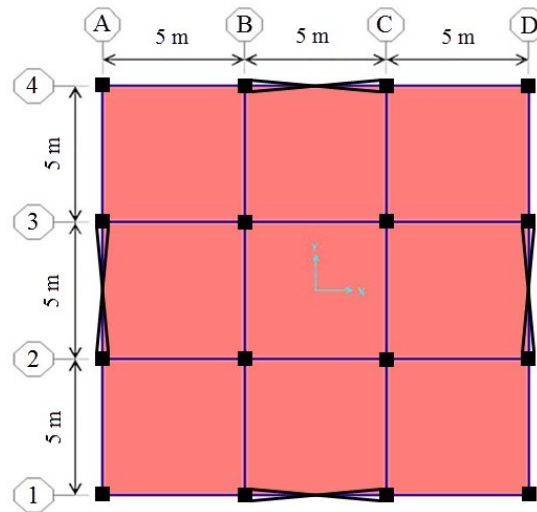
(a)

(b)   (c)

Figure 17. Plan (a) Structure without YOC (b) Structure with YOC (c).

Table 5. Specifications of near-field accelerations [21].

Earthquake Name	Station Name	Date	Magnitude (Richter)	Closest Distance to Fault Rupture (km)	Component	PGA (g)
Imperial Valley	El Centro Array	1979	6.53	0.56	Horizontal-X-axis	0.34
					Horizontal-Y-axis	0.46
					Vertical	0.57
Loma Prieta	LGPC	1989	6.93	3.88	Horizontal-X-axis	0.56
					Horizontal-Y-axis	0.60
					Vertical	0.89
Northridge	Rinaldi Receiving Sta	1994	6.69	6.50	Horizontal-X-axis	0.87
					Horizontal-Y-axis	0.47
					Vertical	0.95

Nejati, F., Zhian, M., Safar Mashaie, F., Edalatpanah, S.A.

Table 6. Specifications of far-field accelerations [21].

Earthquake Name	Station Name	Date	Magnitude (Richter)	Closest Distance to Fault Rupture (km)	Component	PGA (g)
Kobe	Kakogawa	1995	6.90	22.50	Horizontal-X-axis	0.24
					Horizontal-Y-axis	0.32
					Vertical	0.17
Darfield	LPCC	2010	7.00	25.67	Horizontal-X-axis	0.23
					Horizontal-Y-axis	0.35
					Vertical	0.15
Landers	Indio-Jackson Road	1992	7.28	48.84	Horizontal-X-axis	0.30
					Horizontal-Y-axis	0.12
					Vertical	0.08
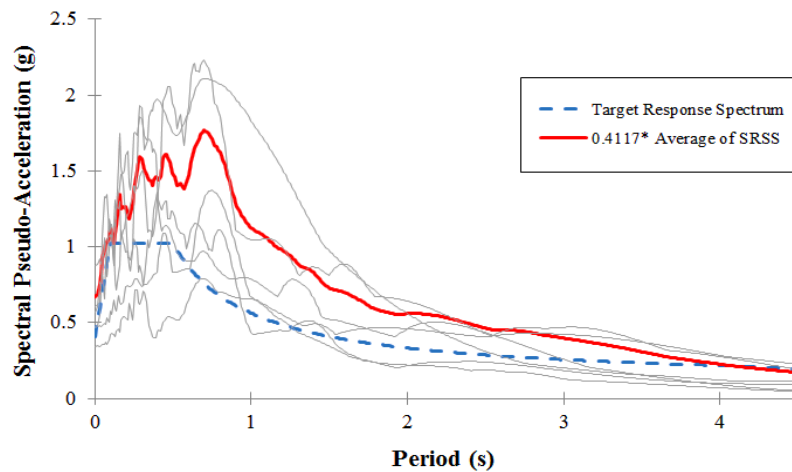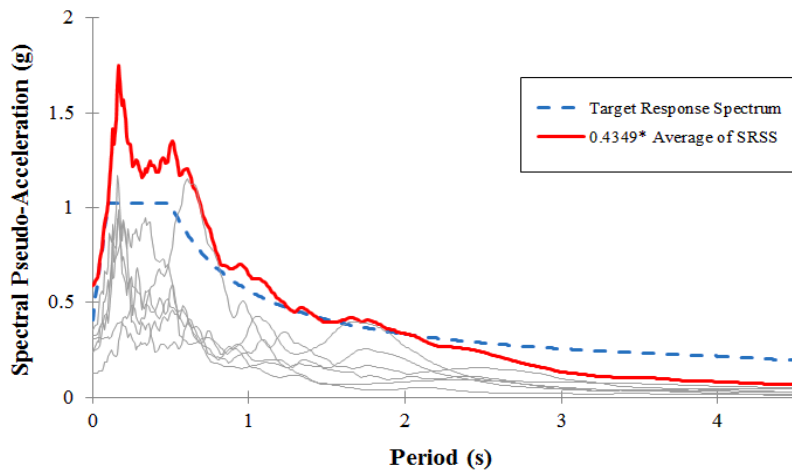
Figure18. Spectral acceleration of the suite of ground motions: near-field (a) far-field (b).

3.   Results and Discussion

To evaluate the effect of using YOC devices in reducing the seismic response, the selected building (Figure 17) equipped with- and without- YOCs is investigated through the non-linear time history analysis and its responses are compared with each other. The results related to the 16-story building are categorized as follows.

3.1. Formation of plastic hinges

Figures 19–24 show how plastic hinges form in the structure equipped with damper and the structure without damper during near- and far-field earthquakes. Evidently, in the structure without damper, plastic hinges are formed until the collapse of the structure. When the braced frame is equipped with the YOCs, no

plastic hinge is formed during the earthquakes; this indicates that the formation of plastic hinges is concentrated on the energy absorption devices and the plasticization of structural members is avoided, and there was no yielding or buckling in the braces.
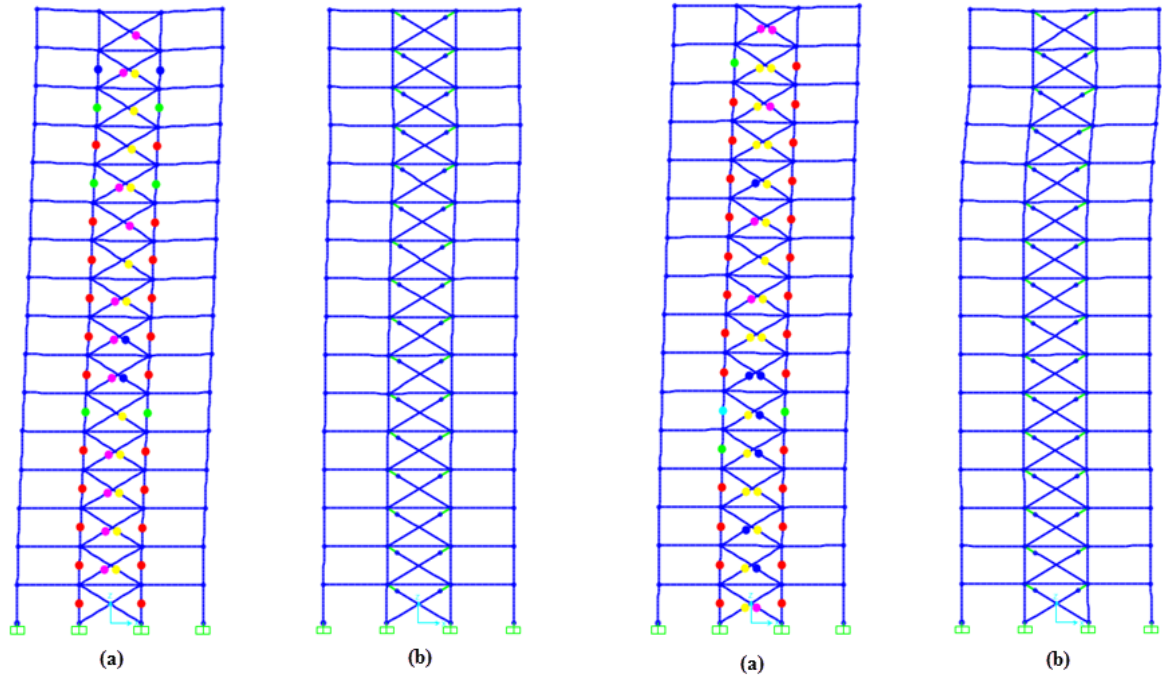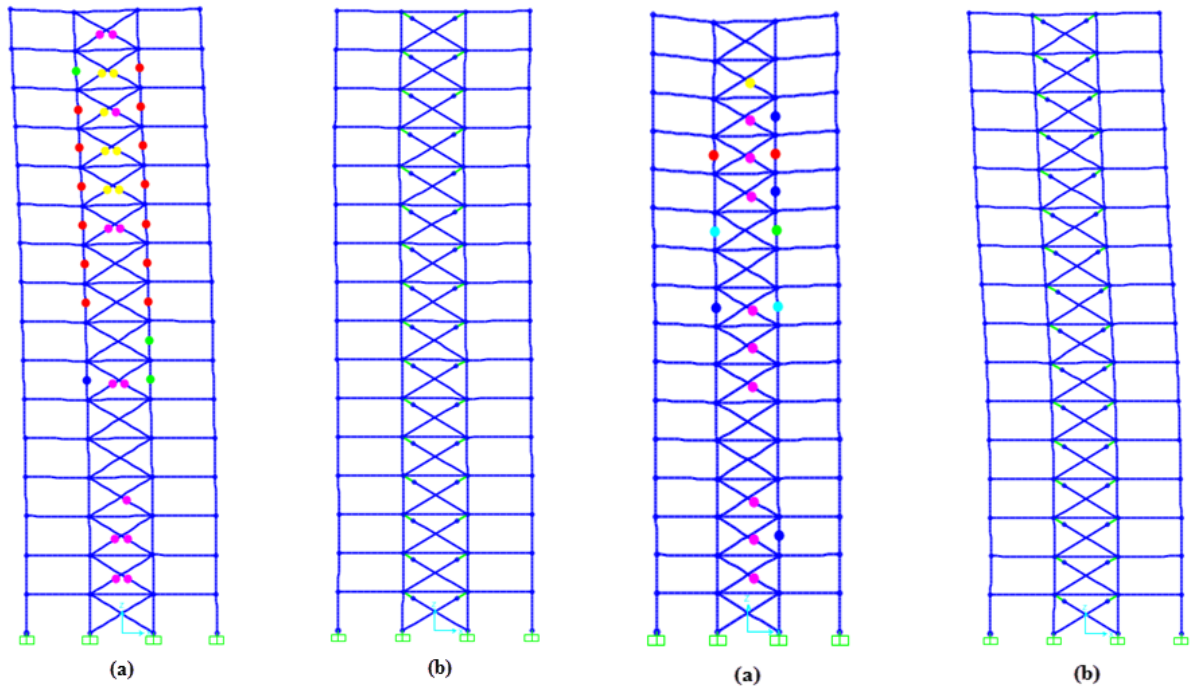

Figure19. Plastic hinges formed subjected to Imperial Valley earthquake: (a) structure without damper; (b) structure equipped with YOCs.

Figure 20. Plastic hinges formed subjected to Loma Prieta earthquake: (a) structure without damper; (b) structure equipped with YOCs.

Figure 21. Plastic hinges formed subjected to Northridge earthquake: (a) structure without damper; (b) structure equipped with YOCs.

Figure 22. Plastic hinges formed subjected to Kobe earthquake: (a) structхлебозаготовиге without damper; (b) structure equipped with YOCs.

3.2. Effect of the damper on story drift ratio

The estimation of the maximum story drift ratio (defined as the ratio of the maximum story drift to the story height) and of the maximum roof displacement is appropriate measures of the global and local response of buildings under earthquakes, respectively. As demonstrated in Figures 25–30, the maximum story drift ratios have an ascending trend in the 16-story structure during the near- and far- field earthquakes. Although the maximum drift ratio in the middle stories increases, it decreases in the upper stories.
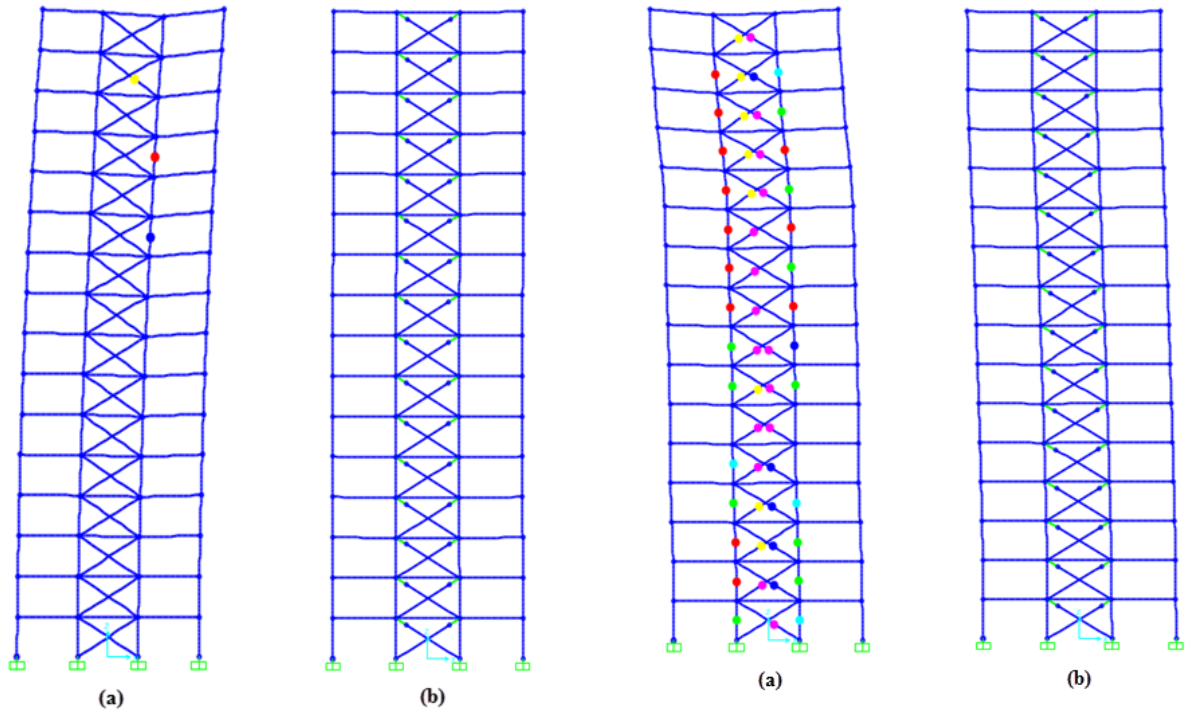
Nejati, F., Zhian, M., Safar Mashaie, F., Edalatpanah, S.A.

Figure 23. Plastic hinges formed subjected to Darfield earthquake: (a) structure without damper; (b) structure equipped with YOCs.

Figure 24. Plastic hinges formed subjected to Landers earthquake: (a) structure without damper; (b) structure equipped with YOCs.
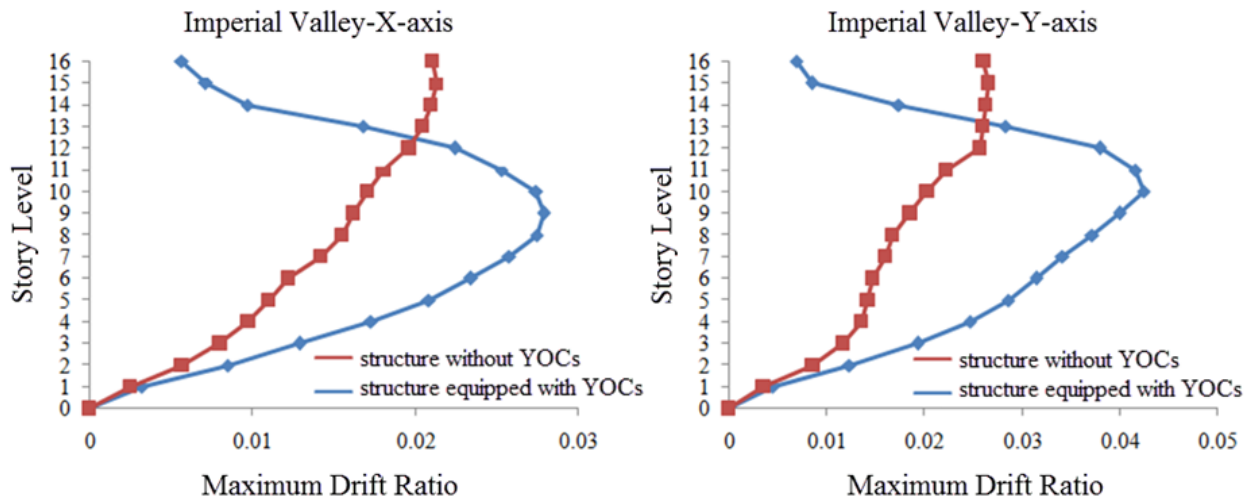

Figure 25. Maximum story drift ratio subjected to Imperial Valley earthquake along X- and Y- axes.
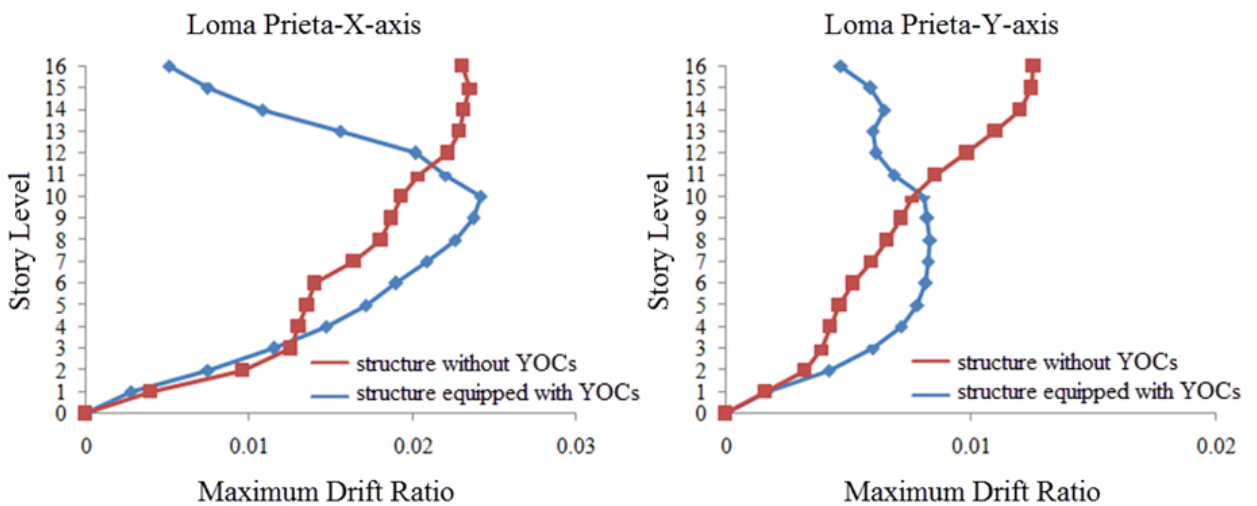

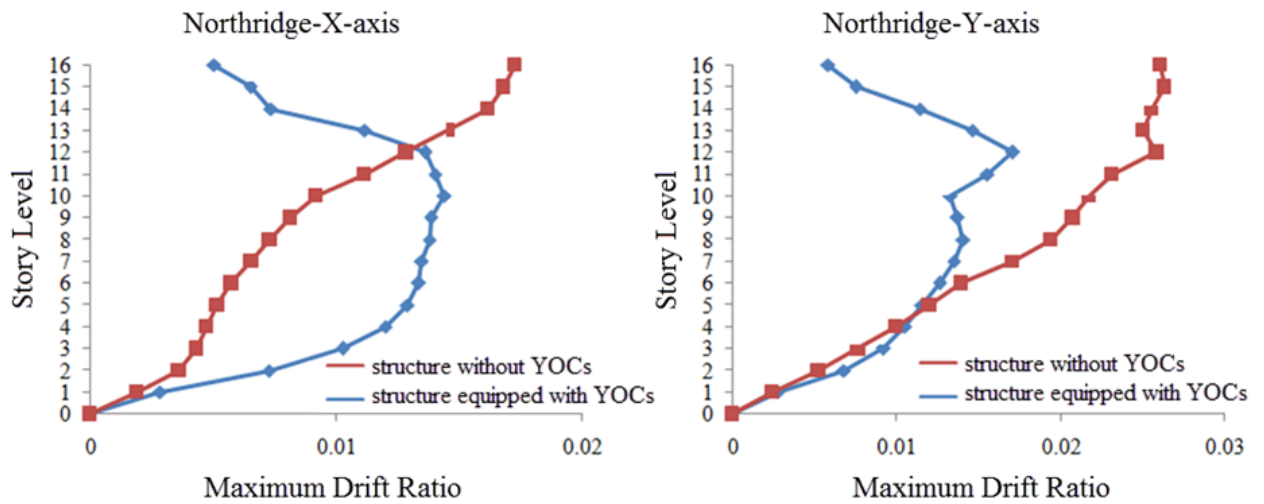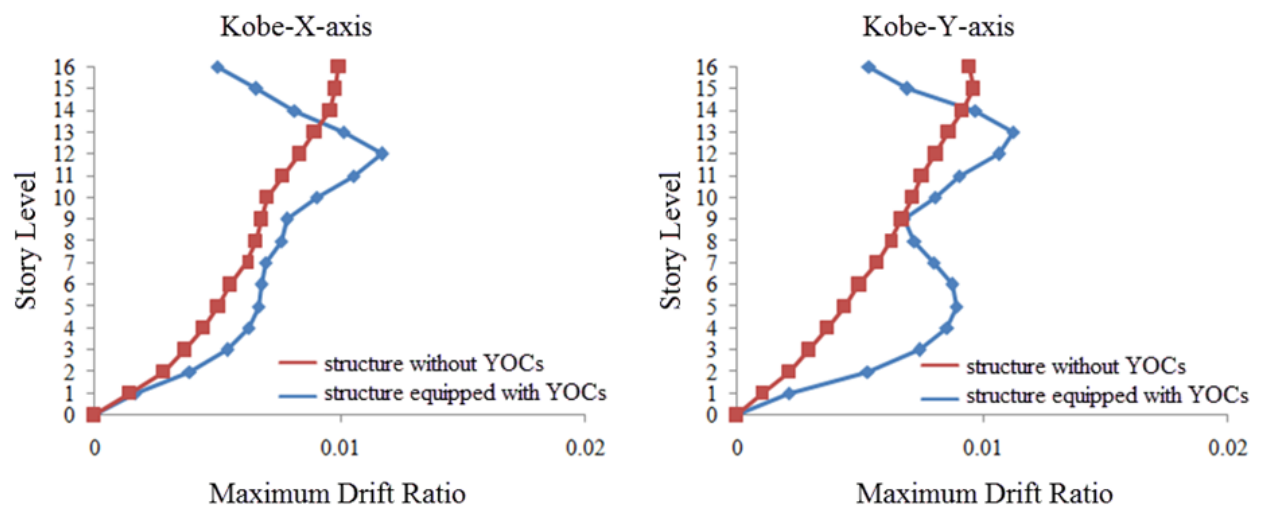**Figure 26. Maximum story drift ratio subjected to Loma Prieta earthquake along X- and Y- axes.**

Nejati, F., Zhian, M., Safar Mashaie, F., Edalatpanah, S.A.

Figure 27. Maximum story drift ratio subjected to Northridge earthquake along X- and Y- axes.

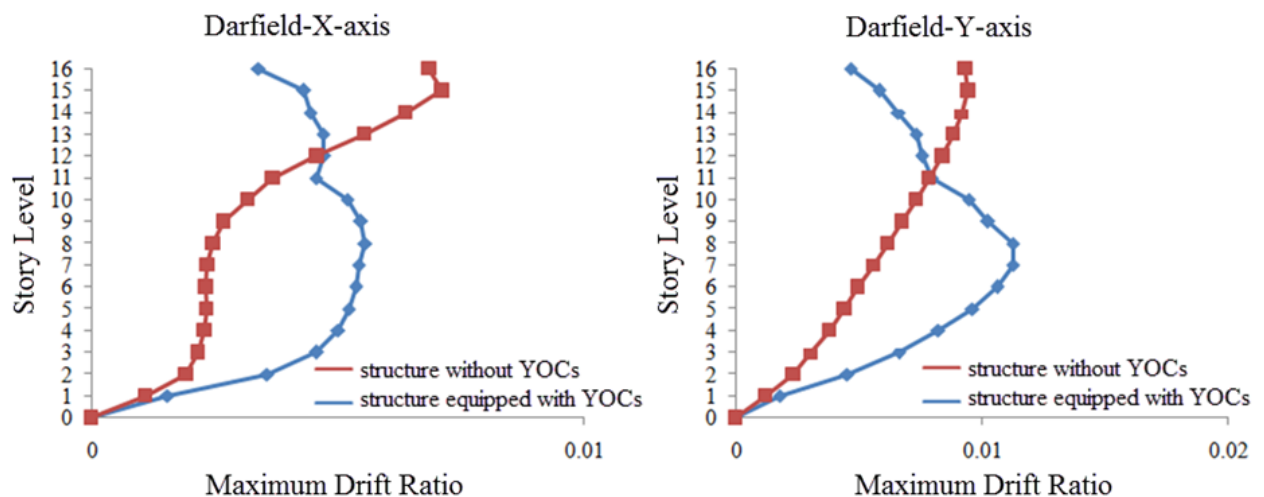**Figure 28. Maximum story drift ratio subjected to Kobe earthquake along X- and Y- axes.**

Figure 29. Maximum story drift ratio subjected to Darfield earthquake along X- and Y- axes.

Usually, the expected loss resulting from damage to acceleration-sensitive non-structural elements is somewhat higher than that in structural elements. Story accelerations are needed for determining forces for the design of non-structural components and equipment supported on the floors. As shown in Figures 31–36 for near- and far-field earthquakes, the peak floor accelerations at all floors of the structure equipped with YOCs are less than that of the structure without YOCs. These results indicate that the performance of non-structural members in the structure equipped with YOCs has improved.
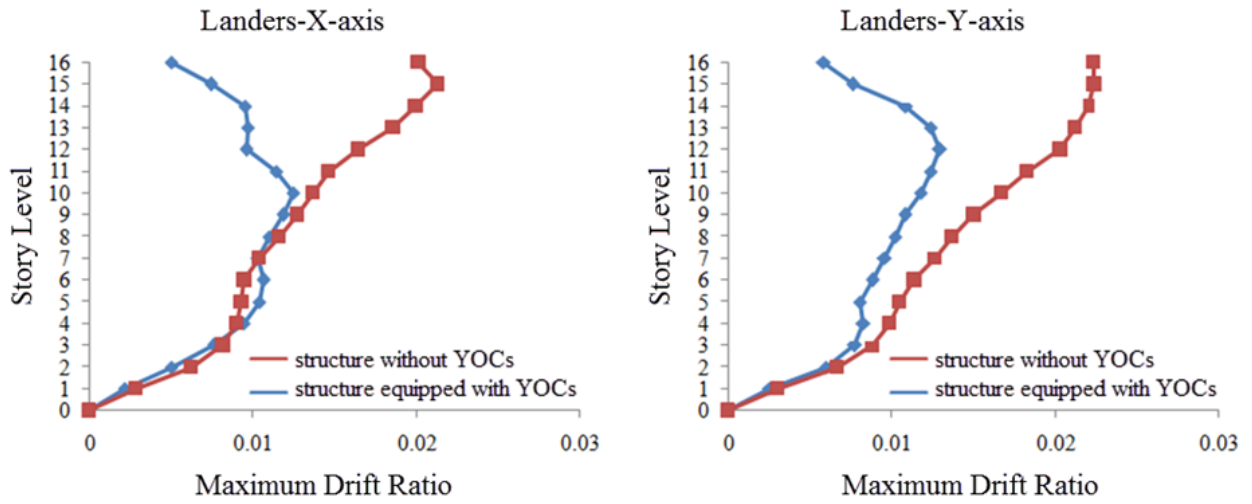
Nejati, F., Zhian, M., Safar Mashaie, F., Edalatpanah, S.A.

Figure 30. Maximum story drift ratio subjected to Landers earthquake along X- and Y- axes.

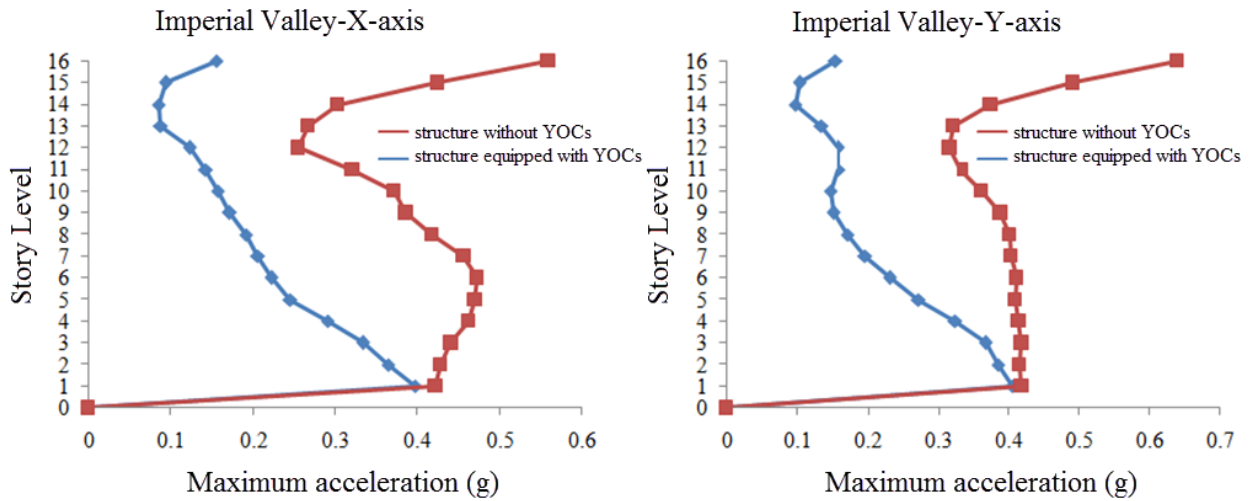### 3.3. Effect of the damper on the peak floor acceleration

Figure 31. Peak floor acceleration ratio subjected to Imperial Valley earthquake along X- and Y- axes.
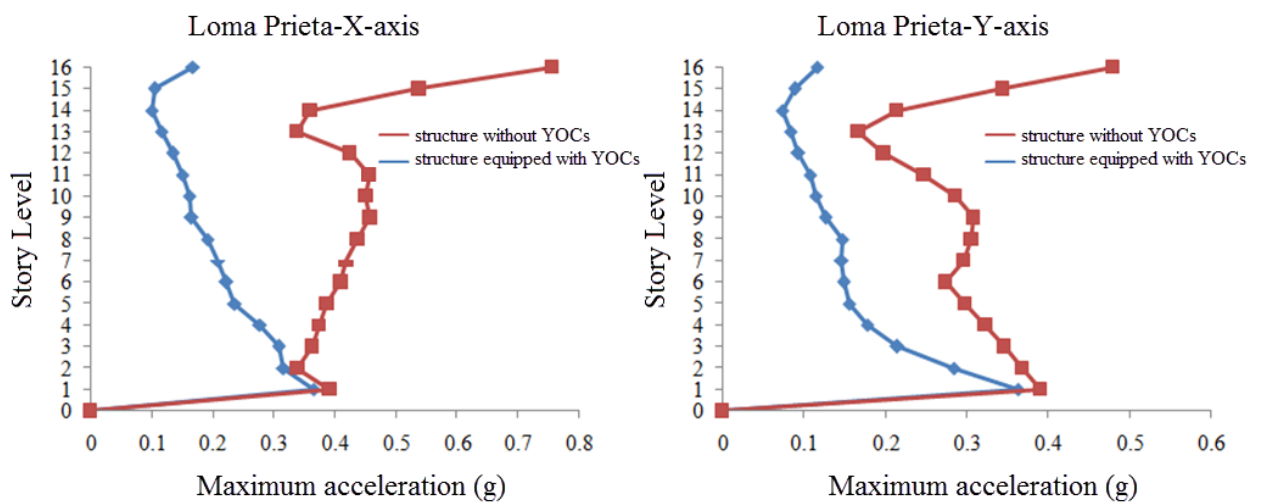

Figure 32. Peak floor acceleration ratio subjected to Loma Prieta earthquake along X- and Y- axes.

In Tables 7 and 8 a comparison of base reaction values in the structure without YOCs and the structure equipped with YOCs is presented and the variations are investigated. The application of YOC in the structure results in a 51–67 % decrease in the base reaction under near-field earthquakes and a 33–65 % decrease in the base reaction under far-field earthquakes. The maximum reduction in the amounts of base reaction for near- and far-field earthquake belongs to the Loma Prieta and Landers earthquakes, respectively.
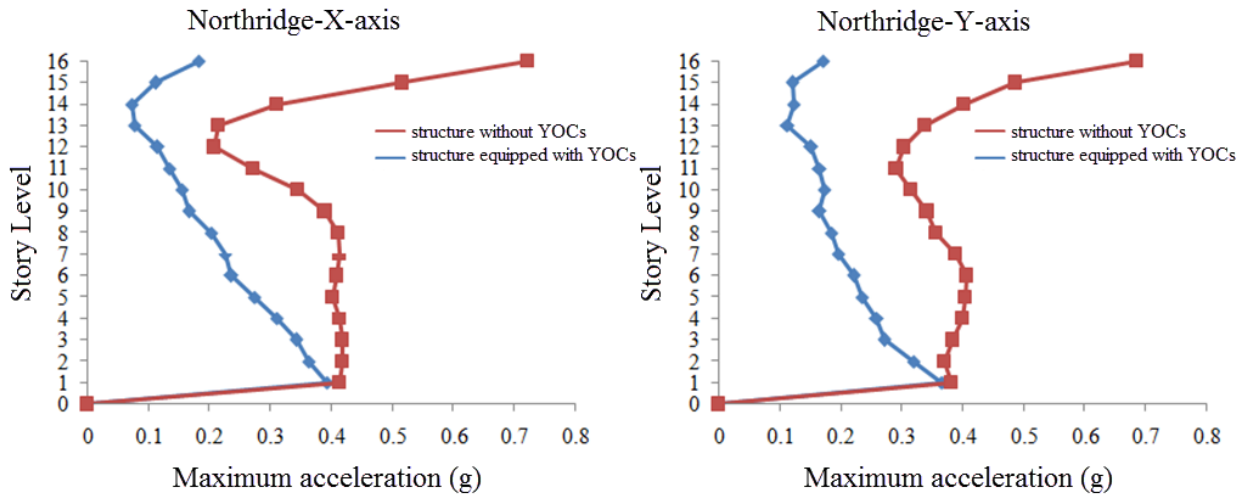
Figure 33. Peak floor acceleration ratio subjected to Northridge earthquake along X- and Y- axes.
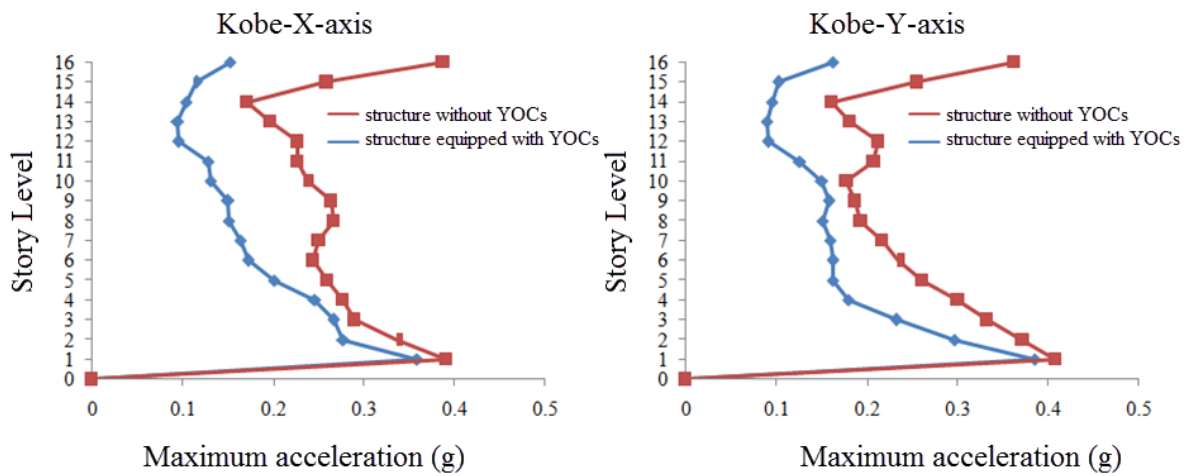

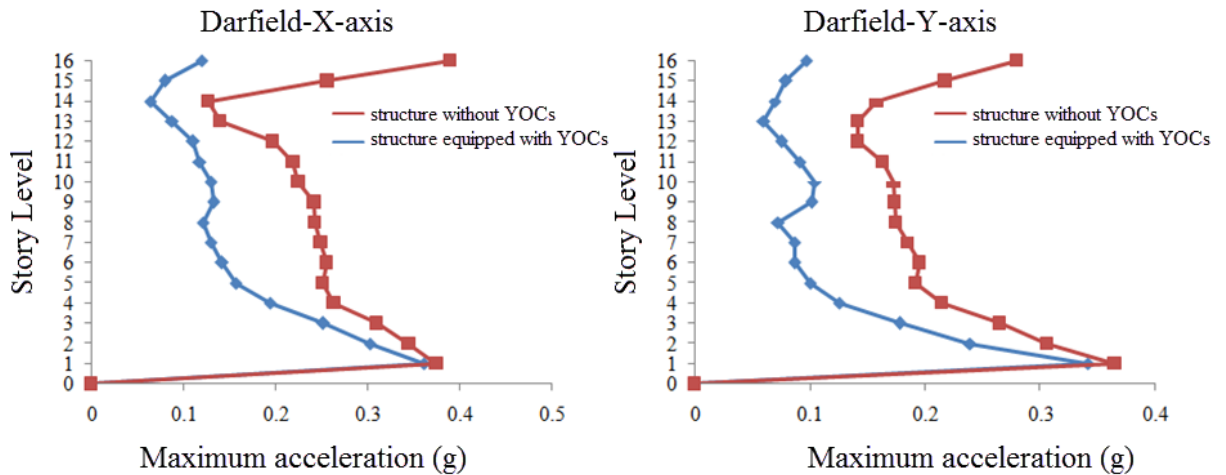Figure 34. Peak floor acceleration ratio subjected to Kobe earthquake along X- and Y- axes.

Figure 35. Peak floor acceleration ratio subjected to Darfield earthquake along X- and Y- axes.

3.4. Effect of the damper on maximum roof acceleration

In Figures 37–42, the time histories of the Peak floor acceleration at roof level during near- and far-field earthquakes are compared. As presented in the acceleration time history graphs, the octagonal damper leads to a significant decrease in the roof acceleration. The reduction of roof acceleration varies from 72 % to 78 % and from 55 % to 82 % under near- and far-field earthquakes, respectively.

3.4.1. Effect of the damper on maximum roof acceleration in near-field earthquakes

It is seen in Figures 37–39 that maximum roof acceleration of the structure equipped with YOCs has decreased by 77 %, 77 % and 75 % of the structure without YOCs under Imperial Valley, Loma Prieta, and Northridge earthquakes, respectively.
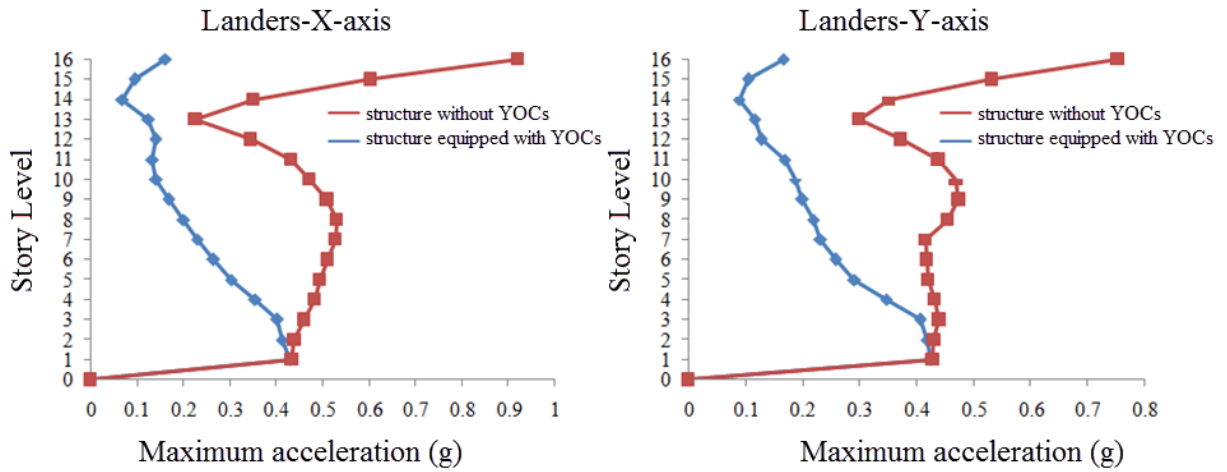
Nejati, F., Zhian, M., Safar Mashaie, F., Edalatpanah, S.A.

47

Figure 36. Peak floor acceleration ratio subjected to Landers earthquake along X- and Y- axes.

3.5. Effect of the damper on base reaction

Table 7. The base reaction of the 16-story building under near-field earthquakes.

Earthquake	Structure equipped with YOCs (ton)		Structure without YOCs (ton)		Difference (%)	
	X-axis	Y-axis	X-axis	Y-axis	X-axis	Y-axis
Imperial Valley	205.99	235.04	502.19	647.06	−58.98	−63.67
Loma Prieta	223.18	151.92	688.33	389.26	−67.57	−60.97
Northridge	237.56	231.81	485.12	540.95	−51.03	−57.14

Table 8. The base reaction of the 16-story building under far-field earthquakes.

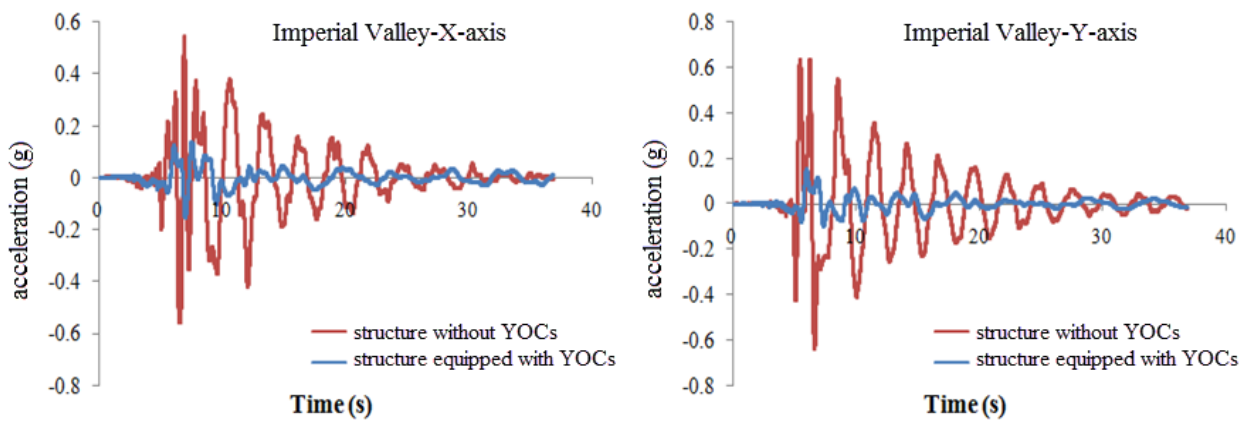| Earthquake	Structure equipped with YOCs (ton)		Structure without YOCs (ton)		Difference (%)	
	X-axis	Y-axis	X-axis	Y-axis	X-axis	Y-axis
Kobe	163.35	159.34	357.69	238.60	−54.33	−33.21
Darfield	142.29	129.53	316.48	300.15	−55.03	−56.84
Landers	240.62	232.61	610.42	675.74	−60.58	−65.57

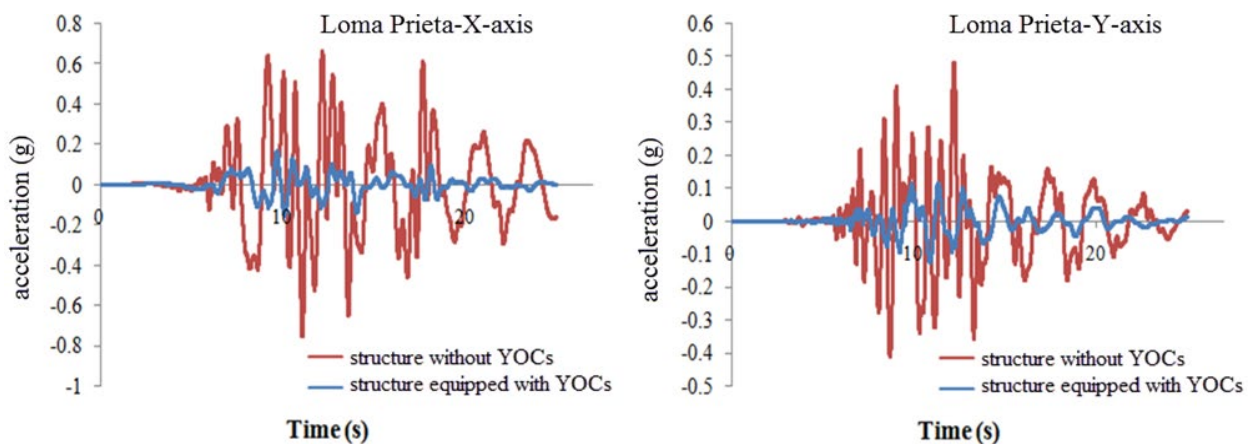**Figure 37. Roof acceleration histories of the building along X- and Y- axes subjected to Imperial Valley earthquake.**

Figure 38. Roof acceleration histories of the building along X- and Y- axes subjected to Loma Prieta earthquake.

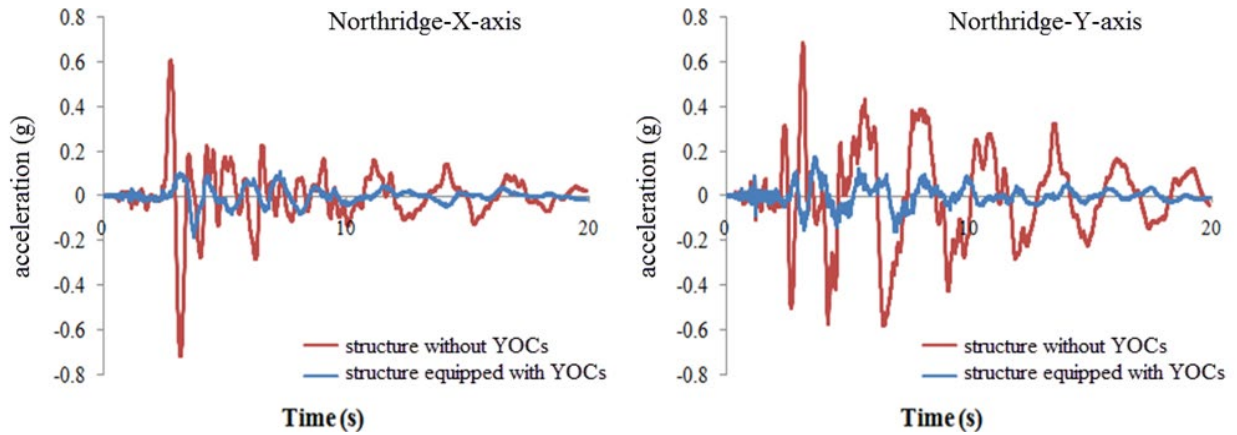Nejati, F., Zhian, M., Safar Mashaie, F., Edalatpanah, S.A.

Figure 39. Roof acceleration histories of the building along X- and Y- axes subjected to Northridge earthquake.

3.5.1. Effect of the damper on maximum roof acceleration in far-field earthquakes

It is seen in Figures 40–42 that maximum roof acceleration of the structure equipped with YOCs has decreased by 62 %, 89 % and 83 % of the structure without YOCs under Kobe, Darfield and Landers earthquakes, respectively. In general, the results of the near- and far field earthquakes indicate that addition of YOC leads to a significant decrease in the maximum acceleration of the roof floor.
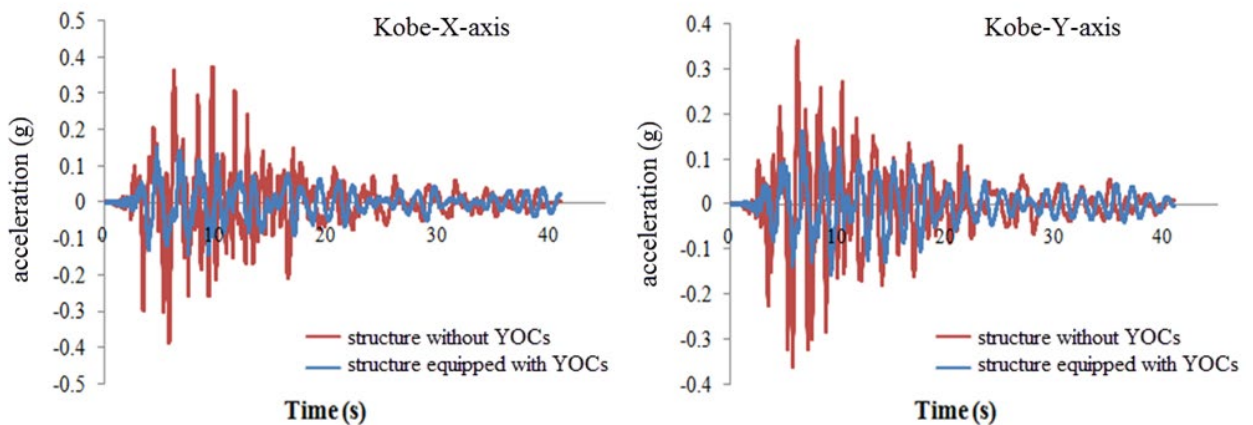

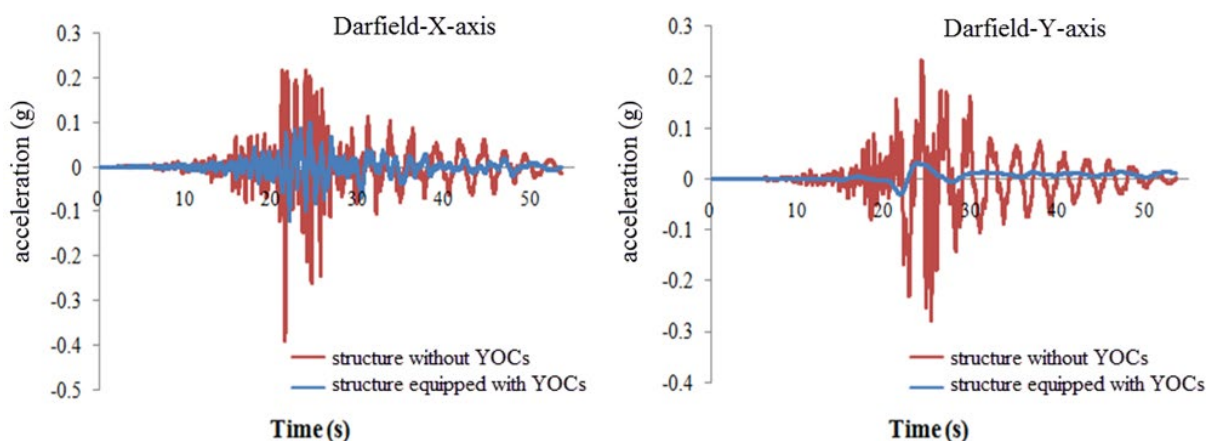**Figure 40. Roof acceleration histories of the building along X- and Y- axes subjected to Kobe earthquake.**

Figure 41. Roof acceleration histories of the building along X- and Y- axes subjected to Darfield earthquake.

3.6. Effect of maximum roof displacement

Figures 43–48 depict the effect of the damper on the time history of the maximum roof displacement during near- and far-field earthquakes. The 16-story structure equipped with the damper can reduce the maximum roof displacement by 61 % under the Northridge earthquake and 57 % under the Landers earthquake. However, an increase of 28 % and 8 % is observed under the Imperial Valley and the Darfield earthquakes, respectively. This difference is due to the fact that the structure shows different behavior under various records.
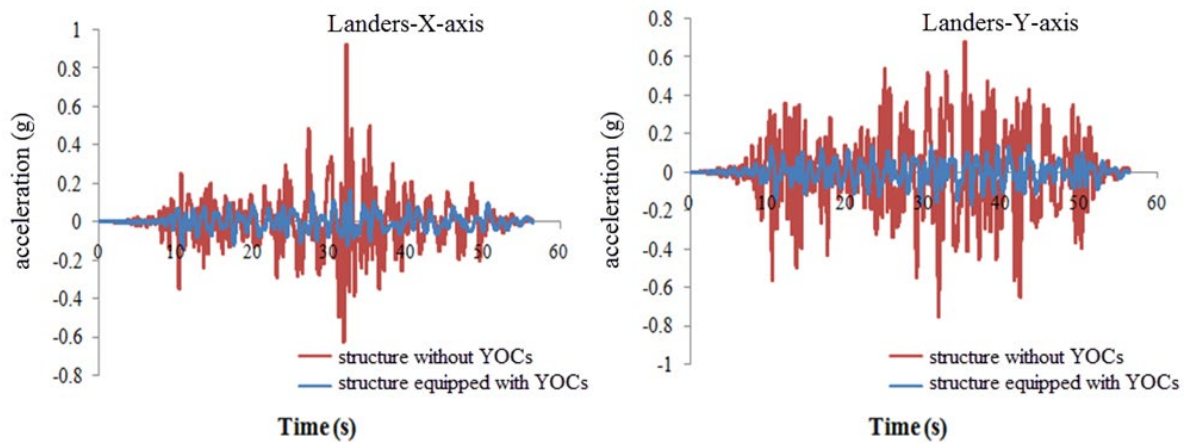
Nejati, F., Zhian, M., Safar Mashaie, F., Edalatpanah, S.A.

Figure 42. Roof acceleration histories of the building along X- and Y- axes subjected to Landers earthquake.

3.6.1. Effect of maximum roof displacement in near-field earthquakes

It can be seen in figures 43 to 45 that maximum roof displacement of the structure equipped with YOCs has decreased by 28 % and 61 % of the structure without YOCs under Loma Prieta and Northridge earthquakes, respectively. It has increased by 28 % under Imperial Valley earthquake.
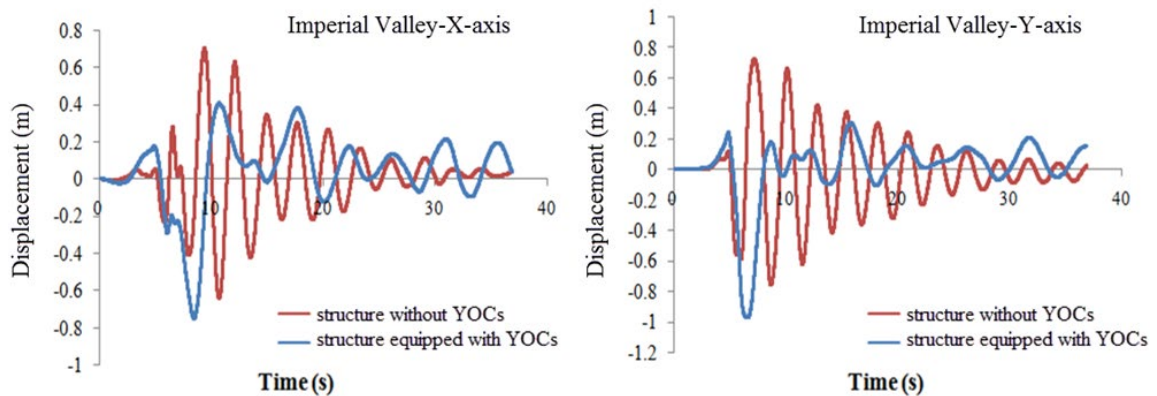

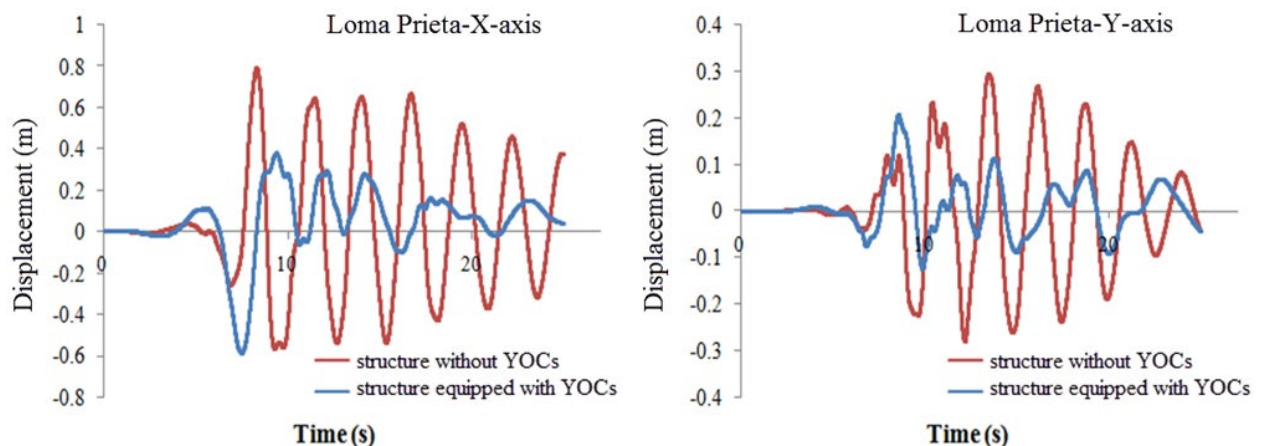**Figure 43. Roof displacement histories of the building along X- and Y- axes subjected to Imperial Valley earthquake.**

Figure 44. Roof displacement histories of the building along X- and Y- axes subjected to Loma Prieta earthquake.

3.6.2. Effect of maximum roof displacement in far-field earthquakes

It can be seen in Figures 46–48 that maximum roof displacement of the structure equipped with YOCs has decreased by 31 % and 58 % of the structure without YOCs under Kobe and Landers earthquakes, respectively. It has increased by 8 % under Darfield earthquake. In general, the results of the near- and far field earthquakes indicate that addition of YOC leads to a decrease in the maximum displacement of the roof floor.
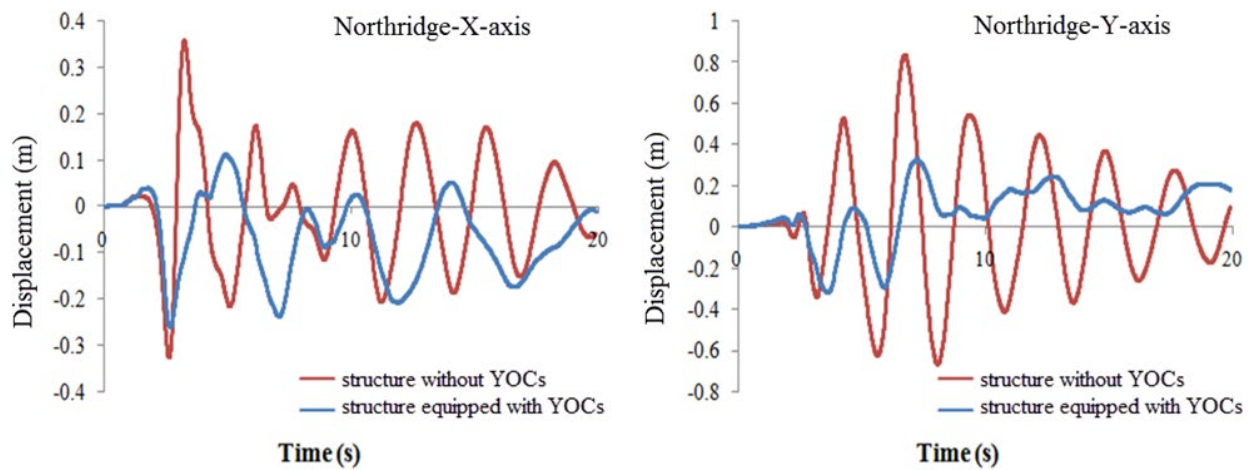
Nejati, F., Zhian, M., Safar Mashaie, F., Edalatpanah, S.A.

Figure 45. Roof displacement histories of the building along X- and Y- axes subjected to Northridge earthquake.
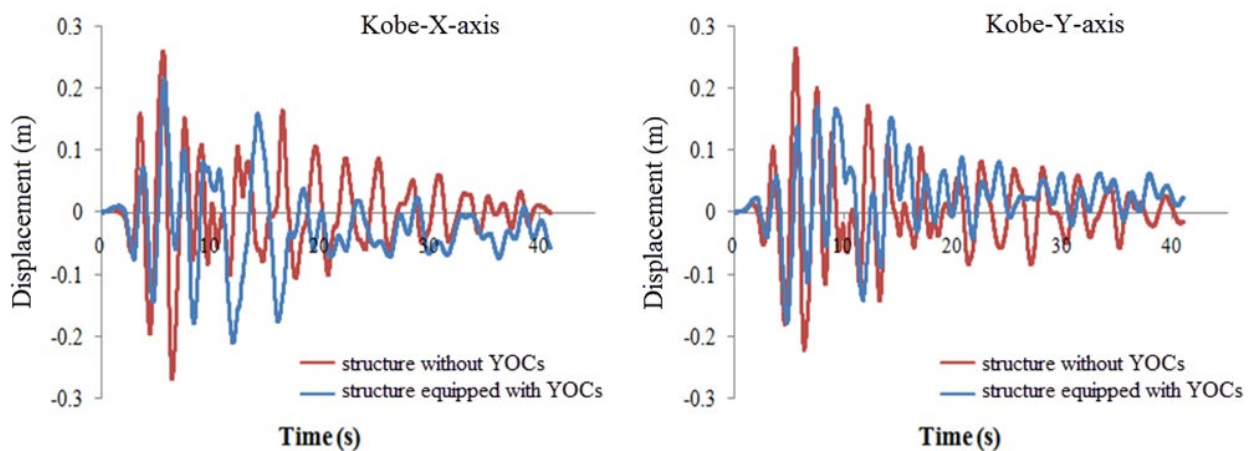

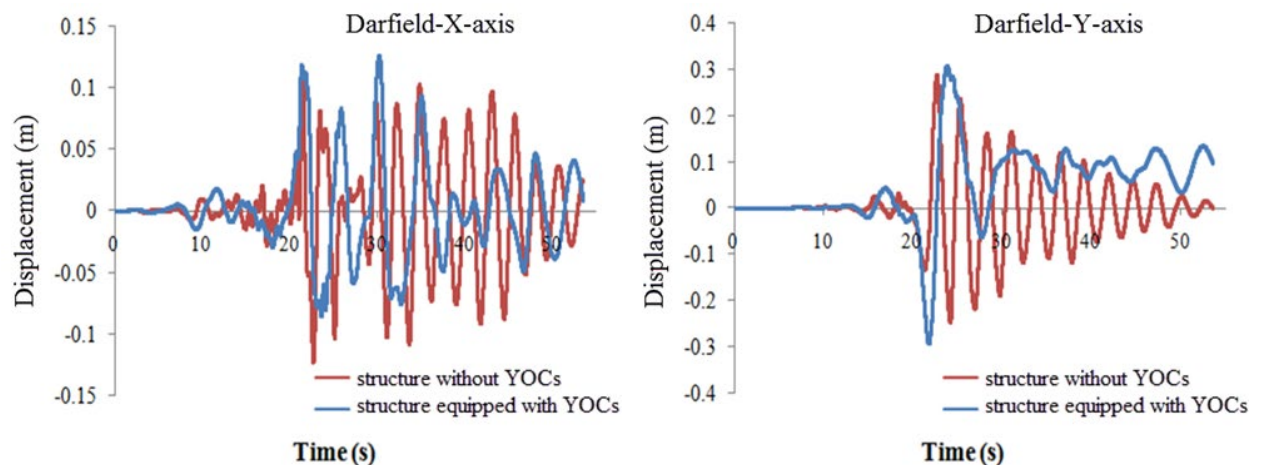**Figure 46. Roof displacement histories of the building along X- and Y- axes subjected to Kobe earthquake.**

Figure 47. Roof displacement histories of the building along X- and Y- axes subjected to Darfield earthquake.

4. Conclusion

In this paper, by using numerical studies, the new energy absorption device on the seismic response of CBF called Yielding Octagonal Connection "YOC" has been introduced, which is modeled using Abaqus finite element software, and hysteresis curve were created for this element under cyclic loading. In order to evaluate the behavior of the YOC, a series of non-linear time history analyses are performed for the 16-story steel structure under near- and far-field earthquakes. Therefore, according to the result of conducted study the following results are presented:
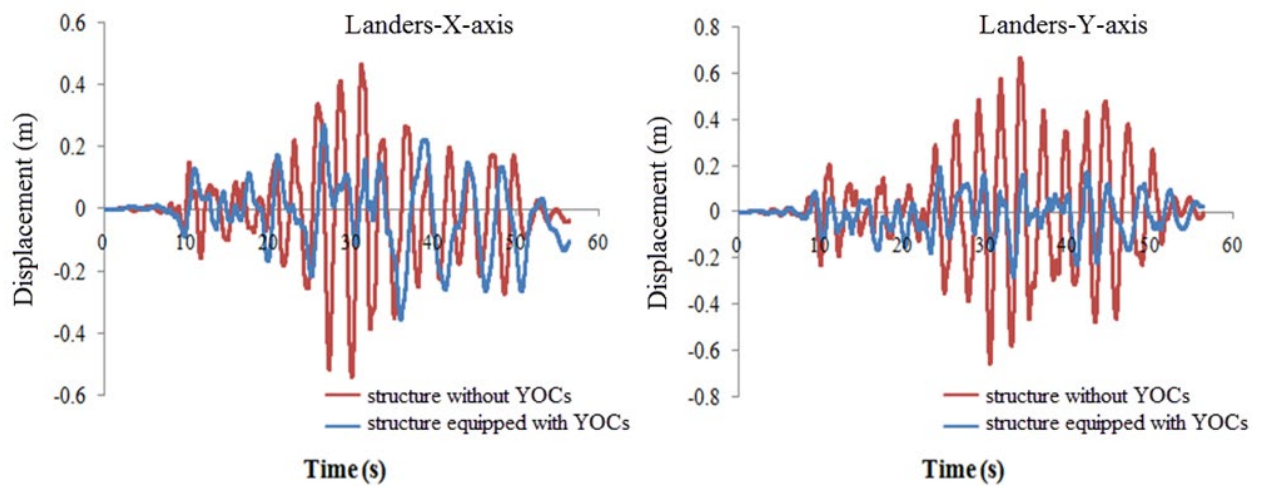
Nejati, F., Zhian, M., Safar Mashaie, F., Edalatpanah, S.A.

Figure 48. Roof displacement histories of the building along X- and Y- axes subjected to Landers earthquake.

• The Non-linear time history analyses performed using the Sap2000 software show that inelastic deformations are concentrated only in the YOCs, and the main structural components were essentially elastic while the structure experienced severe earthquakes. The reason for this is no plastic hinges formed in structural members, and there was no yielding or buckling in the braces.

• Test results show that YOCs are very effective in reducing excessive vibration of the structure due to seismic excitations. The structure equipped with YOC achieves a reduction of the peak floor acceleration in whole stories under near- and far- field earthquakes.

• The analysis findings of the structure containing connection equipped with YOC indicate that although it doesn't keep maximum displacement of stories extent for most of the earthquakes used, it reduces the base reaction to a considerable extent.

• According to the numerical studies carried out in this paper, it was concluded that the amounts of story drift ratios in the structure equipped with YOCs are different under various earthquakes, sometimes are increased or decreased. But the results show that Finally, this study represents a first attempt to describe the cyclic behavior of the proposed YOC numerically. The results of analyzing real structures with such a numerical model can be used to assess design a prototype system for full-scale experimental work. Further studies are necessary to extend experimentally, this scenario for reaching the final goal.

References

1. Franco, J.M., Cahís, X., Gracia, L., López, F. Experimental testing of a new anti-seismic dissipater energy device based on the plasticity of metals. Engineering Structures. 2010. Vol. 32(9). Pp. 2672–2682.

2. Mistakidis, E. Numerical study of low-yield point steel shear walls used for seismic applications. Engineering computations. 2010. Vol. 27(2). Pp. 257–279.

3. Benavent-Climent, A. A brace-type seismic damper based on yielding the walls of hollow structural sections. Engineering Structures. 2010. Vol. 32(4). Pp. 1113–1122.

4. Ward, K.M., Fleischman, R.B., Federico, G.A cast modular bracing system for steel special concentrically braced frames. Engineering Structures. 2012. Vol. 45. Pp. 104–116.

5. Gray, M.G., Christopoulos, C., Packer, J.A. Cast steel yielding brace system for concentrically braced frames: concept development and experimental validations. Journal of Structural Engineering. 2013. Vol. 140(4). 04013095.

6. Beheshti-Aval, S.B., Mahbanouei, H., Zareian, F. A hybrid friction-yielding damper to equip concentrically braced steel frames. International Journal of Steel Structures. 2013. Vol. 13(4). Pp. 577–587.

7. Li, H.N., Li, G. Experimental study of structure with «dual function» metallic dampers. Engineering Structures. 2007. Vol. 29(8). Pp. 1917–1928.

8. Nejati, F., Hosseini, M., Mahmoudzadeh, A. Design of repairable regular steel buildings with square plan based on seesaw motion of building structure and using DADAS dampers. International Journal of Structural Integrity. 2017. Vol. 8(3). Pp. 326–340.

9. Hsu, H.L., Halim, H. Brace performance with steel curved dampers and amplified deformation mechanisms. Engineering Structures. 2018. Vol. 175. Pp. 628–644.

10. Baiguera, M., Vasdravellis, G., Karavasilis, T. L. Dual seismic-resistant steel frame with high post-yield stiffness energy-dissipative braces for residual drift reduction. Journal of Constructional Steel Research. 2016. Vol.122. Pp. 198–212.

11. Taiyari, F., Mazzolani, F.M., Bagheri, S. A proposal for energy dissipative braces with U-shaped steel strips. Journal of Constructional Steel Research. 2019. Vol. 154. Pp. 110–122.

12. Jarrah, M., Khezrzadeh, H., Mofid, M., Jafari, K. Experimental and numerical evaluation of piston metallic damper (PMD). Journal of Constructional Steel Research. 2019. Vol. 154. Pp. 99–109.

13. SAP2000, C. Integrated software for structural analysis and design. Analysis reference manual. Computers and Structures Inc. 2017.

14. ASTM. Standard specification for low and intermediate tensile strength carbon steel plates. ASTM A283/A283M-13, West Conshohocken, PA. 2013.

Nejati, F., Zhian, M., Safar Mashaie, F., Edalatpanah, S.A.

15. ATC24, Guidelines for Cyclic Seismic Testing of Components of Steel Structures. Applied technology council. 1992.

16. FEMA 356. Pre-standard and Commentary for the Seismic Rehabilitation of Buildings. Washington, DC. ASCE Standards Committee on Seismic Rehabilitation. 2000.

17. Abbasnia, R., Vetr, M.G.H., Ahmadi, R., Kafi, M.A. Experimental and analytical investigation on the steel ring ductility. Sharif J. Sci. Technol. 2008. Vol. 52. Pp. 41–48. (Persian)

18. ABAQUS Ver. 6.12, User's Manual, RI, USA. 2012.

19. BHRC. Iranian code of practice for seismic resistant design of buildings: standard No. 2800 (4th. Edition). [Building and Housing Research Center]. 2017. Tehran. 211 p. (Persian)

20. ASCE/SEI Standard 41-13. Seismic Evaluation and of Retrofit of Existing Buildings. Structural Engineering Institute, American society of civil engineers. 2014.

21. PEER Ground Motion Database, Pacific Earthquake Engineering Research Center [Online]. URL: http://ngawest2.berkeley.edu/

Contacts

Faezeh Nejati, civilifa_nj@yahoo.com

Milad Zhian, miladjyane@gmail.com

Fatemeh Safar Mashaie, honik_ir@yahoo.com

Seyyed Ahmad Edalatpanah, saedalatpanah@gmail.com